

Continuous Symmetry Breaking in a Two-dimensional Rydberg Array

Cheng Chen*,¹ Guillaume Borner*,¹ Marcus Bintz*,² Gabriel Emperauer*,¹ Lucas Leclerc,^{1,3} Vincent S. Liu,² Pascal Scholl,^{1,4} Daniel Barredo,^{1,5} Johannes Hauschild,^{2,6,7} Shubhayu Chatterjee,² Michael Schuler,⁸ Andreas M. Läuchli,^{9,10,8} Michael P. Zaletel,^{2,11} Thierry Lahaye,¹ Norman Y. Yao,^{2,11,12} and Antoine Browaeys¹

¹*Université Paris-Saclay, Institut d'Optique Graduate School, CNRS, Laboratoire Charles Fabry, 91127 Palaiseau Cedex, France*

²*Department of Physics, University of California, Berkeley, California 94720 USA*

³*PASQAL SAS, 7 Rue Leonard de Vinci, 91300 Massy, France*

⁴*California Institute of Technology, Pasadena, CA 91125, USA*

⁵*Nanomaterials and Nanotechnology Research Center (CINN-CSIC),*

Universidad de Oviedo (UO), Principado de Asturias, 33940 El Entrego, Spain

⁶*Department of Physics, Technical University of Munich, 85748 Garching, Germany*

⁷*Munich Center for Quantum Science and Technology (MCQST), Schellingstr. 4, D-80799 München, Germany*

⁸*Institut für Theoretische Physik, Universität Innsbruck, A-6020 Innsbruck, Austria*

⁹*Laboratory for Theoretical and Computational Physics, Paul Scherrer Institute, 5232 Villigen, Switzerland*

¹⁰*Institute of Physics, Ecole Polytechnique Fédérale de Lausanne (EPFL), 1015 Lausanne, Switzerland*

¹¹*Materials Sciences Division, Lawrence Berkeley National Laboratory, Berkeley, CA 94720, USA*

¹²*Department of Physics, Harvard University, Cambridge, Massachusetts 02138 USA*

(Dated: July 27, 2022)

Spontaneous symmetry breaking underlies much of our classification of phases of matter and their associated transitions [1–3]. It provides an example of the power of many-body interactions, enabling a collection of individual degrees of freedom to align its behavior across large spatial and temporal scales. Crucially, the nature of the underlying symmetry being broken determines many of the qualitative properties of the phase; this is illustrated by the case of discrete versus continuous symmetry breaking. Indeed, in contrast to the discrete case, the breaking of a continuous symmetry is governed by Goldstone's theorem, which predicts the existence of gapless modes that mediate power-law correlations [4, 5]. In this work, we realize a two-dimensional dipolar XY model – which exhibits a continuous spin-rotational symmetry – utilizing a Rydberg quantum simulator. We demonstrate the adiabatic preparation of correlated low-temperature states of both the XY ferromagnet and the XY antiferromagnet. In the ferromagnetic case, we characterize the presence of long-range XY order, a feature prohibited in absence of the long-range dipolar interaction. Complementing recent works utilizing the Rydberg-blockade mechanism to realize Ising-type interactions (with a discrete spin rotation symmetry) [6–9], our work opens the door to exploring the many-body physics of XY interactions in a programmable quantum simulator.

The collective behavior of many-particle systems can lead to phases of matter that are characterized by the nature of their symmetry breaking [1, 3]. This framework serves to unify a wide variety of phenomena ranging from crystalline and magnetic ordering to superfluidity and superconductivity [10–14]. Constraints on when and how symmetries can be broken abound. For example, long-wavelength fluctuations preclude the breaking of continuous symmetries in low-dimensional systems with short-range interactions [15–21]. The presence of long-range interactions qualitatively alters this picture. On the one hand, long-range interactions can stabilize certain forms of finite-temperature order, which would otherwise be forbidden [22–25]. On the other hand, they can also lead to frustration, where interactions compete with one another, preventing the formation of order [26–30]. Even when order persists in both the short- and long-range cases, the nature of this order, including the dispersion of excitations or the decay of correlation functions, can be fundamentally distinct [24, 31]. Here, we investigate continuous symmetry breaking in a long-range interacting, two-dimensional XY magnet with either ferromagnetic (FM) or antiferromagnetic (AFM) couplings [32–37].

Our experiments are performed on a square lattice of up to $N = 100$ dipolar interacting Rydberg atoms [38] and our

main results are threefold. First, leveraging single-site addressing, we demonstrate the preparation of low-temperature initial states in a staggered magnetic field. By adiabatically decreasing the strength of this field, we can prepare correlated low-temperature states of both the XY ferromagnet and the XY antiferromagnet. Second, we characterize the prepared states by measuring the full spatial profile of the correlation function. In the ferromagnet, the system exhibits correlations consistent with the presence of long-range order – a feature prohibited in conventional short-range-interacting, two-dimensional magnets [12, 17, 18]. Meanwhile, in the antiferromagnet, correlations vanish at long distances, consistent with the decay expected from algebraic long-range order (Fig. 1) [39–43]. Third, by introducing a partial quench into the adiabatic ramp, we tune the effective temperature of the final state. This allows us to probe the finite-temperature phase diagram of the dipolar XY model (Fig. 1).

The experimental setup (Fig. 1a) consists of a two-dimensional square lattice of ^{87}Rb atoms trapped in an optical tweezer array [8]. We encode an effective spin $1/2$ in a pair of opposite-parity Rydberg states, $|\uparrow\rangle = |60S_{1/2}\rangle$ and $|\downarrow\rangle = |60P_{1/2}\rangle$. Resonant dipole-dipole interactions between the spins naturally realize the so-called dipolar XY model

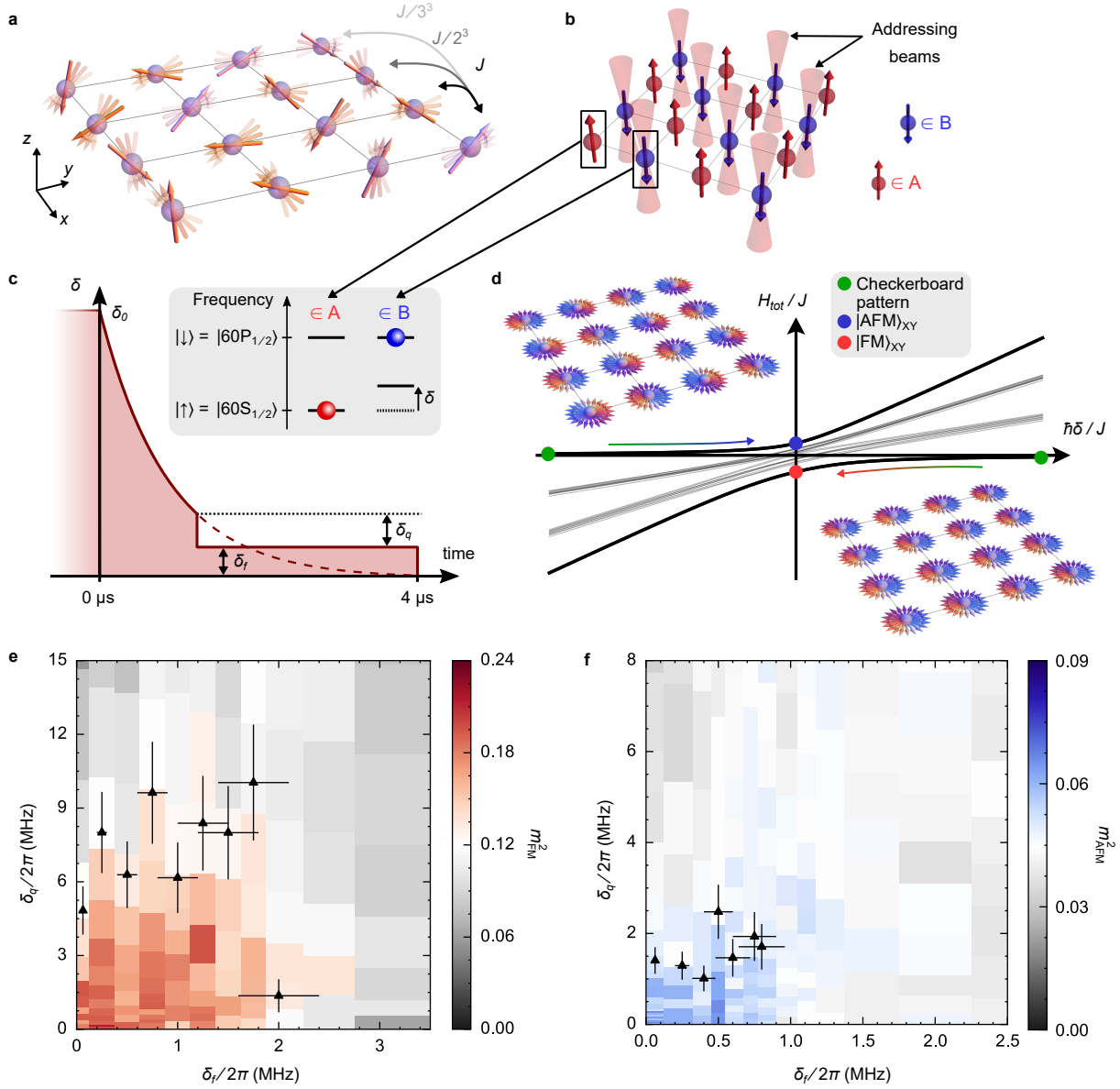


Figure 1. Dipolar XY model in a Rydberg quantum simulator and experimental phase diagram. **a**, Schematic depicting the long-range dipolar XY model. An effective spin is encoded in a pair of Rydberg states which exhibit flip-flop interactions. **b**, A spatially dependent light-shift is used to prepare the system in a Néel configuration. **c**, The amplitude of this Néel pinning field is decreased as a function of time to a final value, δ_f . To study finite temperatures, we introduce an additional diabatic quench of magnitude δ_q . **d**, Energy spectrum of H_{tot} as a function of δ , for $N = 2 \times 3$. When starting in the ground state for $\hbar\delta/J \gg 1$, the system is adiabatically ramped to the ferromagnetic XY state, pictured by the colored fluctuating arrows correlated in directions. On the other hand, when starting in the highest excited state for $\hbar\delta/J \ll -1$, the system is adiabatically ramped to the antiferromagnetic XY state, portrayed by the anticorrelated fluctuating arrows. **e**, Ferromagnetic phase diagram depicting the magnetization squared as a function of the final staggered field strength, δ_f and the diabatic quench magnitude, δ_q (used to control the temperature). Symmetry breaking is expected in a lobe about $(\delta_f = 0, \delta_q = 0)$ and is destroyed by either quantum (δ_f) or thermal (δ_q) fluctuations. On a 6×7 system, a crossover between ordered and disordered behavior is observed. The black triangles indicate the approximate position of the crossover (see Methods Sec. C). Error bars are estimated to 15% of relative uncertainty on the light-shift, due to possible miscalibration and power drifts. **f**, Analogous phase diagram for the antiferromagnet. Note that at finite temperature, only algebraic long-range order is expected.

(Fig. 1a) [38],

$$H_{XY} = -\frac{J}{2} \sum_{i < j} \frac{a^3}{r_{ij}^3} (\sigma_i^x \sigma_j^x + \sigma_i^y \sigma_j^y), \quad (1)$$

where σ_i^α are Pauli matrices, r_{ij} is the distance between spins i and j , $J/\hbar = 0.77$ MHz is the dipolar interaction strength, and $a = 12.5 \mu\text{m}$ is the lattice spacing; here, the quantization axis is defined by an external magnetic field perpendicular to

the lattice plane, which ensures that the dipolar interactions are isotropic. The Hamiltonian exhibits a continuous $U(1)$ symmetry corresponding to the conservation of total magnetization, $M^z = \sum_i \sigma_i^z$ (see Methods Sec. D 1).

We begin by adiabatically preparing low-temperature states of H_{XY} in the $M^z = 0$ sector. To do so, we apply a spatially dependent light-shift, which implements the Hamiltonian, $H_Z = \hbar\delta \sum_i n_i$. The n_i form a checkerboard pattern with $n_i = 0$ on the A-sublattice and $n_i = (1 + \sigma_i^z)/2$ on the B-sublattice (Fig. 1b). Due to the conservation of M^z , this “pinning field” is equivalent (up to a global energy shift) to a staggered magnetic field. For $\hbar|\delta| \gg J$, the ground state (and highest excited state) of the total Hamiltonian $H_{\text{tot}} = H_{XY} + H_Z$, is then, to good approximation, a product state where each spin is aligned (or anti-aligned) along its local z -field – i.e. a classical Néel configuration [44].

The staggered light-shift allows us to prepare a Néel product state (see Methods Sec. B 1) by sweeping a global microwave pulse across the resonance of the A-sublattice spins (Fig. 1b). Starting from the Néel configuration, we then dynamically prepare a variety of highly-correlated, quantum many-body states (for a discussion of an alternative preparation approach, see Methods Sec. E 1). Our main strategy is to ramp down the staggered field as a function of time, either abruptly or adiabatically (Fig. 1c). In the adiabatic case, for $\delta(t) > 0$, the ramp prepares low-temperature ferromagnetic states of H_{XY} . Meanwhile, for $\delta(t) < 0$, so that the initial state is anti-aligned with the local field, the adiabatic ramp prepares *negative* temperature states of H_{XY} or equivalently, low-temperature antiferromagnetic states of $-H_{XY}$ (Fig. 1d) [45]. Note that in the thermodynamic limit of both cases, a quantum phase transition is expected to occur at some critical $\delta_c^{\text{FM/AFM}}$, between the Néel configuration and the XY order (Methods D 3).

To investigate the XY ferromagnet, we begin with a 6×7 lattice and utilize an exponential ramp profile, $\delta(t) \approx \delta_0 e^{-t/\tau}$, with $\delta_0 = 2\pi \times 15$ MHz and $\tau = 0.3 \mu\text{s}$. As depicted in Fig. 2a, for both sublattices, the on-site z -magnetization decreases toward zero, with a residual late-time offset arising from experimental imperfections (see Methods Sec. B 2). This is consistent with the XY ferromagnet, which orders in the equatorial plane, but by itself, is insufficient to diagnose the phase. Indeed, quenching the staggered field (in less than 100 ns) leads to a near infinite temperature state, which also exhibits a magnetization that rapidly relaxes to zero (lighter curves, Fig. 2a).

The key characteristic of the XY ferromagnet is only revealed upon measuring the correlation function, $C_{ij}^x = \langle \sigma_i^x \sigma_j^x \rangle - \langle \sigma_i^x \rangle \langle \sigma_j^x \rangle$ (Methods D 1). For the quenched state, the correlation functions remain near zero for all times, consistent with high-temperature behavior (lighter curves, Fig. 2b). The dynamics of the adiabatic protocol are markedly distinct – both nearest-neighbor and next-nearest-neighbor correlations grow to a non-zero plateau value at late times, indicative of order [12]. By switching the sign of δ_0 , we also investigate the XY antiferromagnet. Both the z -magnetization (Fig. 2d) and the correlation functions (Fig. 2e) exhibit qualitatively similar dynamics as the ferromagnetic case. Crucially

however, as expected for an antiferromagnet, C^x flips sign between the nearest- and next-nearest-neighbor correlations.

A few remarks are in order. First, to explore the adiabaticity of our protocol, we vary the time-constant of the exponential ramp. As shown in the insets of Fig. 2b,e, the dynamics of the correlation function agree between $\tau = 0.15 \mu\text{s}$ and $\tau = 0.3 \mu\text{s}$, indicating that diabatic errors are not a limiting factor. We confirm this by numerical simulation of the many-body dynamics (see Methods Fig. 11). Second, for a nearest-neighbor XY model, it is well-known that the ferromagnet and antiferromagnet are directly related by a sublattice rotation [5]. In the presence of long-range interactions, this is no longer the case. In particular, the long-range tail of the dipolar interactions becomes weakly frustrated for the antiferromagnet. As a consequence, the phase transition between the Néel configuration and the XY antiferromagnet is expected to occur at a smaller value of the staggered field as compared to the XY ferromagnet, i.e. $|\delta_c^{\text{AFM}}| < |\delta_c^{\text{FM}}|$ (see also Methods Sec. E). This is indeed borne out by the data where we observe that the magnetization decays to zero faster as a function of δ for the ferromagnetic case than for the antiferromagnet. Third, we increase the system size to a 10×10 lattice and perform the analogous adiabatic preparation protocols. We find the same behavior for all observables (insets, Fig. 2a,d), indicating that our results are robust to finite-size effects [46, 47]. Finally, we note that at the latest times, the correlations in both the ferromagnetic and antiferromagnetic cases exhibit a slow decay; we conjecture that this decay arises from a combination of residual atomic motion and the finite lifetime of the Rydberg states (more details in Methods B 2).

To characterize the nature of the XY order in both the FM and the AFM, we measure the long-distance spatial correlations of the system after adiabatic preparation. In Fig. 2c,f [6 \times 7] and Fig. 3a [10 \times 10] we show the two-point correlations as a function of the displacement \vec{d} , averaging over initial positions: $C^x(\vec{d}) \equiv \langle C_{\vec{r}, \vec{r}+\vec{d}}^x \rangle_{\vec{r}}$. The ferromagnetic correlations are of constant sign and appear to plateau at long distances, indicative of long-range order, while the antiferromagnetic correlations are staggered and exhibit a decay.

To investigate this behavior more quantitatively, we focus on the 10×10 lattice and plot $C^x(d)$, averaging over displacements of the same distance $d = |\vec{d}|$. The XY ferromagnet indeed exhibits a plateau, $C^x \sim 0.13$, corresponding to an in-plane magnetization density of $m = \sqrt{2C^x} = 0.51$. On the other hand, the XY antiferromagnet exhibits a decay to zero at large distances indicating the absence of long-range order. We note that running the adiabatic preparation protocol to longer timescales leads to additional decoherence which adversely affects the ferromagnetic magnetization plateau in a non-trivial fashion; in particular, correlations at the largest distances begin to decay before their shorter-distance counterparts (see Methods B 2). Finally, in Fig. 3b, we compare the measured $C^x(d)$ against the exact ground-state prediction obtained from density matrix renormalization group calculations (see Methods Sec. D 2) [48, 49]. While the qualitative structure of $C^x(d)$ (e.g. sign structure in the AFM case) is consistent with theory, the experimental correlations are weaker.

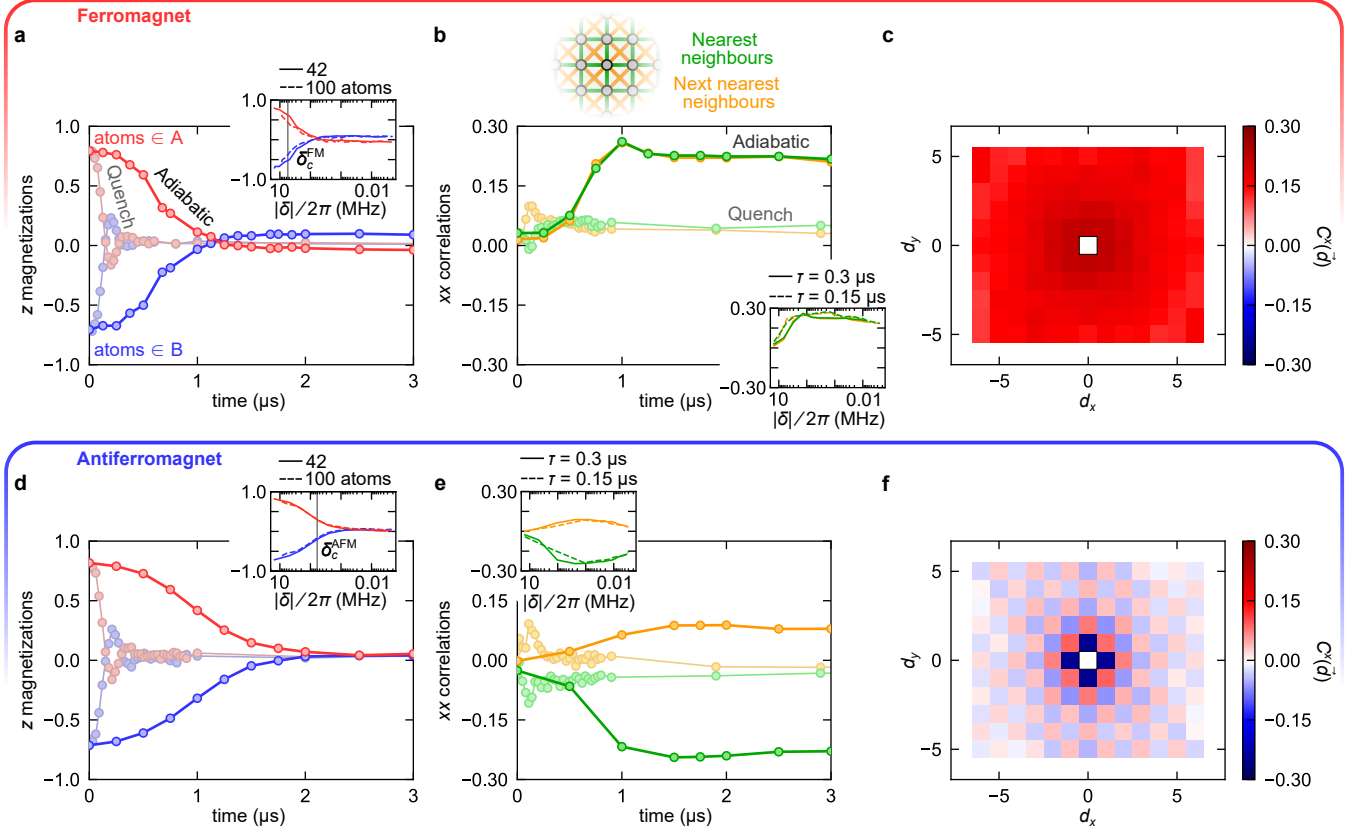


Figure 2. **Adiabatic preparation of dipolar XY ferro- and antiferromagnets.** **a**, Sublattice-resolved magnetization $\langle \sigma_i^z \rangle$ as the staggered field $\delta(t)$ is reduced. At $t = 0$, the state is prepared in a classical Néel state along the z -axis, as indicated by the opposing magnetization of atoms in the A (red) and B (blue) sublattices. As the staggered field $\delta(t)$ is turned off, either adiabatically or via a sudden quench, the Néel magnetization decays towards zero. (inset) Comparison of the z -magnetizations decay as a function of δ for a 6×7 versus a 10×10 lattice. The gray vertical line indicates the value δ_c^{FM} where the phase transition occurs, inferred from the theory (Methods D 2). **b**, The formation of a low-entropy XY-ferromagnet is detected via the in-plane two-point correlation function, C_{ij}^x . Data is shown for i, j averaged over either nearest or next-nearest pairs. The sudden quench produces additional entropy which destroys the XY order and leads to correlations near zero. (inset) Nearest and next-nearest correlations for two different adiabatic ramp rates. **c**, xx correlations as a function of displacement, $C^x(\vec{d}) \equiv \langle C_{\vec{r}, \vec{r}+\vec{d}}^x \rangle_{\vec{r}}$, measured at time, $t = 2 \mu\text{s}$ (with d_x and d_y in units of lattice spacing a). **d-f**, Analogous results for the antiferromagnetic case. Crucially (**e,f**), we observe staggered correlations.

A number of effects could contribute to this. For example, the finite fidelity of the initial Néel product state introduces an entropy density, which is not accounted for in ground state calculations. The effect of additional experimental imperfections including readout errors and decoherence are discussed in the Methods, Sec. B; including these errors in our numerical simulations leads to excellent agreement with the data for the 6×7 lattice (see Methods Fig. 10).

Thus far, we have focused on adiabatic ramps, with the aim of preparing the ground state at $\delta = 0$. Let us now turn to exploring the phase diagram of the dipolar XY model as a function of temperature and the final value of the staggered field, $\delta = \delta_f$. In order to tune the effective temperature, we introduce a partial quench of amplitude δ_q into the ramp, followed by an equilibration time of at least $1 \mu\text{s}$ (Fig. 1d). The intuition behind our approach is the following: the variable quench introduces excess energy into the system, which thermalizes during the equilibration time, leading to the prepara-

tion of a higher-temperature state. We will use the amplitude of the quench, δ_q , as a proxy for the final temperature. After each $\{\delta_f, \delta_q\}$ ramp, we measure the in-plane magnetization squared, $m_{\text{FM/AFM}}^2 = \sum_{ij} (\pm 1)^{d_x+d_y} C_{ij}^x / N^2$. Starting with the ferromagnet, for small values of δ_f and δ_q (corresponding to low temperatures), there is an $\mathcal{O}(1)$ magnetization per site, consistent with the ordered phase (Fig. 1e). As either δ_f or δ_q increases, the magnetization density decreases toward zero indicating melting into a disordered phase. This is consistent with theoretical expectations, where δ_q drives the transition via thermal fluctuations [23], while δ_f tunes across the quantum phase transition (see Methods Sec. F).

Quantitatively determining the thermodynamic phase boundary would require systematically increasing the system size in order to perform a scaling analysis [47]. In practice, this is challenging due to the limited power of the laser used to apply the light-shift δ (Methods A 1), and the need for slower adiabatic preparation in larger systems (Methods E 1).

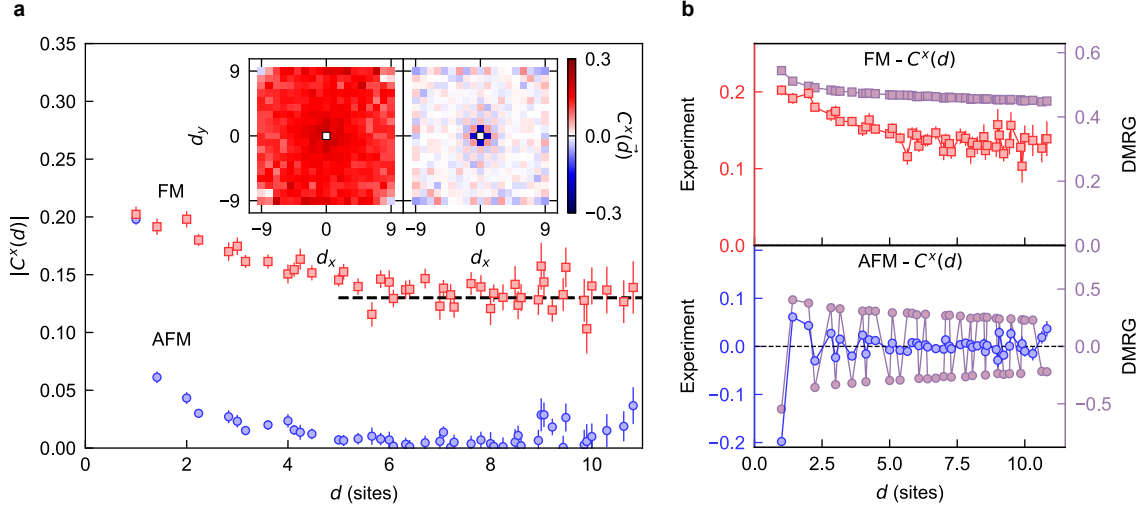


Figure 3. **Observing long-range XY order in a 10×10 lattice.** **a**, xx correlations averaging over displacements of the same distance, $C^x(d)$. The XY ferromagnet exhibits a plateau consistent with long-range order, while the XY antiferromagnet exhibits a decay to zero. (inset) Spatial correlations as a function of displacement, measured at time $t = 1 \mu\text{s}$. **b**, Comparison of the experimental data shown in **a** with the ground-state results obtained from DMRG.

As a proxy for this analysis, in Fig. 1e, we indicate the crossover where m_{FM}^2 reaches an arbitrary threshold (Methods C), which reveals an ordered region about $\{\delta_f = 0, \delta_q = 0\}$. Interestingly, it appears that the “critical” value of δ_q is not monotonic as a function of δ_f . This may be because the entropy produced during the quench depends non-linearly on δ_f (Methods F). We perform the same analysis for the antiferromagnet (Fig. 1f). Compared to the XY ferromagnet, we find that a much smaller region of the $\{\delta_f, \delta_q\}$ phase space exhibits significant AFM correlations, consistent with the frustration induced by the long-range interactions.

Discussion – Our observations are consistent with several non-trivial theoretical expectations arising from the long-range nature of the dipolar interaction. Recall that in the ferromagnetic case, $1/r^3$ interactions circumvent the usual no-go criteria for finite-temperature continuous symmetry breaking in two dimensions [23, 24, 31]. This is consistent with our observation of a plateau in the ferromagnetic $C^x(d)$ for small $\{\delta_f, \delta_q\}$. In contrast, theory predicts that dipolar interactions are insufficient to stabilize finite temperature, long-range order in the antiferromagnetic case [21, 31]. Rather, one expects power-law decaying, algebraic long-range order due to Berezinskii-Kosterlitz-Thouless physics [39–43]. This is consistent with the absence of an observed plateau, although the demonstration of a power-law will require future experiments able to scale to larger system sizes. Note that while long-range AFM order is theoretically possible at zero temperature, our $\delta_q = 0$ ramp does not realize this limit because the finite fidelity of the initial Néel state places a lower bound on the achievable temperature.

Outlook – Looking forward, our work opens the door to a number of intriguing future directions. First, it would be interesting to investigate the nature of the phase transition between the disordered and XY-ordered phases; this will require overcoming a number of technical challenges including scaling to

larger system sizes. Second, the ability to directly prepare low-temperature states in different M^z magnetization sectors suggests the possibility of directly observing the so-called Anderson tower of states, which underlies continuous symmetry breaking [10, 13, 14, 50]; the structure of these states has led to recent predictions for scalable spin squeezing by quenching in the ferromagnetic XY phase [51]. Finally, combining optical tweezer geometries which exhibit frustration (i.e. triangular or kagome lattices) with antiferromagnetic interactions leads to a rich landscape for exploring frustrated magnetism and spin liquid physics [26, 28].

ACKNOWLEDGMENTS

We acknowledge the insights of and discussions with M. Aidesburger, L. Henriot, V. Lienhard, J. Moore, C. Laumann, B. Halperin, E. Altman, B. Ye, E. Davis, and M. Block. We are especially indebted to Hans Peter Büchler for insightful comments and discussions about the role of dipolar-interactions in the XY model. The computational results presented were performed in part using the FASRC Cannon cluster supported by the FAS Division of Science Research Computing Group at Harvard University, the Savio computational cluster resource provided by the Berkeley Research Computing program at the University of California, Berkeley and the Vienna Scientific Cluster (VSC). This work is supported by the European Union’s Horizon 2020 research and innovation program under grant agreement No. 817482 (PASQuanS), the Agence Nationale de la Recherche (ANR, project RYBOTIN), and the European Research Council (Advanced grant No. 101018511-ATARAXIA). J.H. acknowledges support from the NSF OIA Convergence Accelerator Program under award number 2040549, and the Munich Quantum Valley, which is supported by the Bavarian state government with funds

from the Hightech Agenda Bayern Plus. MS and AML acknowledge support by the Austrian Science Fund (FWF) through Grant No. I 4548. DB acknowledges support from MCIN/AEI/10.13039/501100011033 (RYC2018- 025348-I, PID2020-119667GA-I00, and European Union NextGenerationEU PRTR-C17.I1) M.Z. acknowledges support from the DOE Early Career program and the Alfred P. Sloan foundation. N.Y.Y. acknowledges support from the Army Research Office (W911NF-21-1-0262), the AFOSR MURI pro-

gram (W911NF-20-1-0136), the David and Lucile Packard foundation, and the Alfred P. Sloan foundation. M.B. and V.L. acknowledge support from NSF QLCI program (grant no. OMA-2016245). S.C. acknowledges support from the ARO through the MURI program (grant number W911NF-17-1-0323) and from the U.S. DOE, Office of Science, Office of Advanced Scientific Computing Research, under the Accelerated Research in Quantum Computing (ARQC) program.

-
- [1] L. D. Landau, On the theory of phase transitions. I., *Zh. Eksp. Teor. Fiz.* **11**, 19 (1937).
 - [2] L. D. Landau and V. L. Ginzburg, On the theory of superconductivity, *Zh. Eksp. Teor. Fiz.* **20**, 1064 (1950).
 - [3] J. Kepler, *De Nive Sexangula* (Gottfried Tampach, Frankfurt, 1611).
 - [4] J. Goldstone, Field theories with “Superconductor” solutions, *Il Nuovo Cimento* **19**, 154 (1961).
 - [5] H. Tasaki, *Physics and Mathematics of Quantum Many-Body Systems*, Graduate Texts in Physics (Springer International Publishing, Cham, 2020).
 - [6] P. Schauß, J. Zeiher, T. Fukuhara, S. Hild, M. Cheneau, T. Macrì, T. Pohl, I. Bloch, and C. Gross, Crystallization in ising quantum magnets, *Science* **347**, 1455 (2015).
 - [7] E. Guardado-Sanchez, P. T. Brown, D. Mitra, T. Devakul, D. A. Huse, P. Schauß, and W. S. Bakr, Probing the quench dynamics of antiferromagnetic correlations in a 2D quantum Ising spin system, *Phys. Rev. X* **8**, 021069 (2018).
 - [8] P. Scholl, M. Schuler, H. J. Williams, A. A. Eberharter, D. Barredo, K.-N. Schymik, V. Lienhard, L.-P. Henry, T. C. Lang, T. Lahaye, A. M. Läuchli, and A. Browaeys, Quantum simulation of 2D antiferromagnets with hundreds of Rydberg atoms, *Nature* **595**, 233 (2021).
 - [9] S. Ebadi, T. T. Wang, H. Levine, A. Keesling, G. Semeghini, A. Omran, D. Bluvstein, R. Samajdar, H. Pichler, W. W. Ho, S. Choi, S. Sachdev, M. Greiner, V. Vuletić, and M. D. Lukin, Quantum phases of matter on a 256-atom programmable quantum simulator, *Nature* **595**, 227 (2021).
 - [10] P. W. Anderson, An Approximate Quantum Theory of the Antiferromagnetic Ground State, *Physical Review* **86**, 694 (1952).
 - [11] J. Bardeen, L. N. Cooper, and J. R. Schrieffer, Theory of Superconductivity, *Physical Review* **108**, 1175 (1957).
 - [12] C. N. Yang, Concept of off-diagonal long-range order and the quantum phases of liquid He and of superconductors, *Reviews of Modern Physics* **34**, 694 (1962).
 - [13] P. W. Anderson, *Basic Notions of Condensed Matter Physics*, 10th ed., Advanced Book Classics (Perseus Publ, Cambridge, Mass, 2010).
 - [14] A. Beekman, L. Rademaker, and J. van Wezel, An introduction to spontaneous symmetry breaking, *SciPost Physics Lecture Notes*, **11** (2019).
 - [15] F. Bloch, Zur Theorie des Ferromagnetismus, *Zeitschrift für Physik* **61**, 206 (1930).
 - [16] R. Peierls, Quelques propriétés typiques des corps solides, *Annales de l’institut Henri Poincaré* **5**, 177 (1935).
 - [17] N. D. Mermin and H. Wagner, Absence of Ferromagnetism or Antiferromagnetism in One- or Two-Dimensional Isotropic Heisenberg Models, *Physical Review Letters* **17**, 1133 (1966).
 - [18] P. C. Hohenberg, Existence of Long-Range Order in One and Two Dimensions, *Physical Review* **158**, 383 (1967).
 - [19] N. D. Mermin, Crystalline order in two dimensions, *Physical Review* **176**, 250 (1968).
 - [20] J. Fröhlich and C. Pfister, On the absence of spontaneous symmetry breaking and of crystalline ordering in two-dimensional systems, *Communications in Mathematical Physics* **81**, 277 (1981).
 - [21] P. Bruno, Absence of Spontaneous Magnetic Order at Nonzero Temperature in One- and Two-Dimensional Heisenberg and XY Systems with Long-Range Interactions, *Physical Review Letters* **87**, 137203 (2001).
 - [22] F. J. Dyson, Existence of a phase-transition in a one-dimensional Ising ferromagnet, *Communications in Mathematical Physics* **12**, 91 (1969).
 - [23] H. Kunz and C. E. Pfister, First order phase transition in the plane rotator ferromagnetic model in two dimensions, *Communications in Mathematical Physics* **46**, 245 (1976).
 - [24] S. V. Maleev, Dipole forces in two-dimensional and layered ferromagnets, *Soviet Journal of Experimental and Theoretical Physics* **43**, 1240 (1976).
 - [25] J. Fröhlich, R. Israel, E. H. Lieb, and B. Simon, Phase transitions and reflection positivity. I. General theory and long range lattice models, *Communications in Mathematical Physics* **62**, 1 (1978).
 - [26] H. T. Diep, ed., *Frustrated Spin Systems*, 2nd ed. (World Scientific, New Jersey, 2013).
 - [27] C. Castelnovo, R. Moessner, and S. L. Sondhi, Magnetic monopoles in spin ice, *Nature* **451**, 42 (2008).
 - [28] N. Y. Yao, M. P. Zaletel, D. M. Stamper-Kurn, and A. Vishwanath, A quantum dipolar spin liquid, *Nature Physics* **14**, 405 (2018).
 - [29] A. Keleş and E. Zhao, Absence of Long-Range Order in a Triangular Spin System with Dipolar Interactions, *Physical Review Letters* **120**, 187202 (2018).
 - [30] A. Keleş and E. Zhao, Renormalization group analysis of dipolar Heisenberg model on square lattice, *Physical Review B* **97**, 245105 (2018).
 - [31] D. Peter, S. Müller, S. Wessel, and H. P. Büchler, Anomalous behavior of spin systems with dipolar interactions, *Physical Review Letters* **109**, 025303 (2012).
 - [32] P. Richerme, Z.-X. Gong, A. Lee, C. Senko, J. Smith, M. Foss-Feig, S. Michalakakis, A. V. Gorshkov, and C. Monroe, Non-local propagation of correlations in quantum systems with long-range interactions, *Nature* **511**, 198 (2014).
 - [33] P. Jurcevic, B. P. Lanyon, P. Hauke, C. Hempel, P. Zoller, R. Blatt, and C. F. Roos, Quasiparticle engineering and entanglement propagation in a quantum many-body system, *Nature* **511**, 202 (2014).
 - [34] B. Yan, S. A. Moses, B. Gadway, J. P. Covey, K. R. A. Hazzard, A. M. Rey, D. S. Jin, and J. Ye, Observation of dipolar spin-exchange interactions with lattice-confined polar molecules,

- Nature* **501**, 521 (2013).
- [35] L. Christakis, J. S. Rosenberg, R. Raj, S. Chi, A. Morn-ingstar, D. A. Huse, Z. Z. Yan, and W. S. Bakr, Probing site-resolved correlations in a spin system of ultracold molecules, [arXiv:2207.09328](#) (2022).
 - [36] L. Chomaz, I. Ferrier-Barbut, F. Ferlaino, B. Laburthe-Tolra, B. L. Lev, and T. Pfau, Dipolar physics: A review of experiments with magnetic quantum gases, [arXiv:2201.02672](#) (2022).
 - [37] N. Leo, S. Holenstein, D. Schildknecht, O. Sendetskyi, H. Luetkens, P. M. Derlet, V. Scagnoli, D. Lançon, J. R. L. Mardegan, T. Prokscha, A. Suter, Z. Salman, S. Lee, and L. J. Heyderman, Collective magnetism in an artificial 2D XY spin system, *Nature Communications* **9**, 2850 (2018).
 - [38] A. Browaeys and T. Lahaye, Many-body physics with individually controlled Rydberg atoms., *Nature Physics* **16**, 132 (2020).
 - [39] V. L. Berezinskii, Destruction of Long-range Order in One-dimensional and Two-dimensional Systems having a Continuous Symmetry Group I. Classical Systems, *Soviet Journal of Experimental and Theoretical Physics* **32**, 493 (1971).
 - [40] V. L. Berezinskii, Destruction of Long-range Order in One-dimensional and Two-dimensional Systems Possessing a Continuous Symmetry Group. II. Quantum Systems, *Soviet Journal of Experimental and Theoretical Physics* **34**, 610 (1972).
 - [41] J. M. Kosterlitz and D. J. Thouless, Ordering, metastability and phase transitions in two-dimensional systems, *Journal of Physics C: Solid State Physics* **6**, 1181 (1973).
 - [42] J. M. Kosterlitz, The critical properties of the two-dimensional XY model, *Journal of Physics C: Solid State Physics* **7**, 1046 (1974).
 - [43] G. Giachetti, N. Defenu, S. Ruffo, and A. Trombettoni, Berezinskii-Kosterlitz-Thouless Phase Transitions with Long-Range Couplings, *Physical Review Letters* **127**, 156801 (2021).
 - [44] L. Néel, Propriétés magnétiques de l'état métallique et énergie d'interaction entre atomes magnétiques, *Annales de physique* **11**, 232 (1936).
 - [45] A. S. Sørensen, E. Altman, M. Gullans, J. V. Porto, M. D. Lukin, and E. Demler, Adiabatic preparation of many-body states in optical lattices, *Physical Review A* **81**, 061603 (2010).
 - [46] P. Hasenfratz and F. Niedermayer, Finite size and temperature effects in the AF Heisenberg model, *Zeitschrift für Physik B Condensed Matter* **92**, 91 (1993).
 - [47] A. W. Sandvik and C. J. Hamer, Ground-state parameters, finite-size scaling, and low-temperature properties of the two-dimensional $S = 1/2$ XY model, *Physical Review B* **60**, 6588 (1999).
 - [48] S. R. White, Density matrix formulation for quantum renormalization groups, *Physical Review Letters* **69**, 2863 (1992).
 - [49] J. Hauschild and F. Pollmann, Efficient numerical simulations with Tensor Networks: Tensor Network Python (TeNPy), *SciPost Physics Lecture Notes*, **5** (2018).
 - [50] H. Tasaki, Long-Range Order, “Tower” of States, and Symmetry Breaking in Lattice Quantum Systems, *Journal of Statistical Physics* **174**, 735 (2019).
 - [51] T. Comparin, F. Mezzacapo, and T. Roscilde, Robust spin squeezing from the tower of states of $U(1)$ -symmetric spin Hamiltonians, *Physical Review A* **105**, 022625 (2022).
 - [52] D. Barredo, S. de Léséleuc, V. Lienhard, T. Lahaye, and A. Browaeys, An atom-by-atom assembler of defect-free arbitrary 2d atomic arrays, *Science* **354**, 1021 (2016).
 - [53] S. de Léséleuc, D. Barredo, V. Lienhard, A. Browaeys, and T. Lahaye, Analysis of imperfections in the coherent optical excitation of single atoms to Rydberg states, *Physical Review A* **97**, 053803 (2018).
 - [54] T. Kennedy, E. H. Lieb, and B. S. Shastri, The XY Model Has Long-Range Order for All Spins and All Dimensions Greater than One, in *Statistical Mechanics*, edited by B. Nachtergaele, J. P. Solovej, and J. Yngvason (Springer Berlin Heidelberg, Berlin, Heidelberg, 1988) pp. 327–329.
 - [55] J. E. Björnberg and D. Ueltschi, Reflection positivity and infrared bounds for quantum spin systems, [arXiv:2204.12896](#) (2022).
 - [56] In preparation.
 - [57] E. Stoudenmire and S. R. White, Studying Two-Dimensional Systems with the Density Matrix Renormalization Group, *Annual Review of Condensed Matter Physics* **3**, 111 (2012).
 - [58] M. B. Hastings and T. Koma, Spectral Gap and Exponential Decay of Correlations, *Communications in Mathematical Physics* **265**, 781 (2006).
 - [59] V. Lienhard, S. de Léséleuc, D. Barredo, T. Lahaye, A. Browaeys, M. Schuler, L.-P. Henry, and A. M. Läuchli, Observing the space- and time-dependent growth of correlations in dynamically tuned synthetic Ising antiferromagnets, *Physical Review X* **8**, 021070 (2018).
 - [60] S. de Léséleuc, V. Lienhard, P. Scholl, D. Barredo, S. Weber, N. Lang, H. P. Büchler, T. Lahaye, and A. Browaeys, Observation of a symmetry-protected topological phase of interacting bosons with Rydberg atoms, *Science* **365**, 775 (2019).
 - [61] P. J. Jensen, K. H. Bennemann, D. K. Morr, and H. Dreyssé, Two-dimensional Heisenberg antiferromagnet in a transverse field, *Physical Review B* **73**, 144405 (2006).
 - [62] S. Kar, K. Wierschem, and P. Sengupta, Magnons in a two-dimensional transverse-field XXZ model, *Physical Review B* **96**, 045126 (2017).
 - [63] S.-J. Gu, Fidelity approach to quantum phase transitions, *International Journal of Modern Physics B* **24**, 4371 (2010).
 - [64] M. P. Zaletel, R. S. K. Mong, C. Karrasch, J. E. Moore, and F. Pollmann, Time-evolving a matrix product state with long-ranged interactions, *Physical Review B* **91**, 165112 (2015).
 - [65] J. Tobochnik and G. V. Chester, Monte Carlo study of the planar spin model, *Physical Review B* **20**, 3761 (1979).
 - [66] A. Ueda and M. Oshikawa, Resolving the Berezinskii-Kosterlitz-Thouless transition in the two-dimensional XY model with tensor-network-based level spectroscopy, *Physical Review B* **104**, 165132 (2021).
 - [67] H.-Q. Ding and M. S. Makivić, Kosterlitz-Thouless transition in the two-dimensional quantum XY model, *Physical Review B* **42**, 6827 (1990).
 - [68] H.-Q. Ding, Phase transition and thermodynamics of quantum XY model in two dimensions, *Physical Review B* **45**, 230 (1992).
 - [69] S. Romano, Computer simulation study of a long-range plane-rotator system in two dimensions, *Nuovo Cim, B* **100**, 447 (1987).
 - [70] S. Romano, Computer-simulation study of a disordered plane-rotator system in two dimensions with long-range ferromagnetic interactions, *Physical Review B* **42**, 8647 (1990).
 - [71] O. F. Syljuåsen and A. W. Sandvik, Quantum Monte Carlo with directed loops, *Physical Review E* **66**, 046701 (2002).

METHODS

A. Experimental methods

The realization of the dipolar XY model relies on our ^{87}Rb Rydberg-atom tweezer array setup, described in previous works [8, 52]. The pseudo-spin states are $|\uparrow\rangle = |60S_{1/2}, m_J = 1/2\rangle$ and $|\downarrow\rangle = |60P_{1/2}, m_J = -1/2\rangle$. We manipulate them using resonant microwaves at 16.7 GHz. A ~ 40 -G magnetic field, perpendicular to the array, defines the quantization axis (Fig. 4a) and shifts away the irrelevant Zeeman states of the $60S_{1/2}$ and $60P_{1/2}$ manifolds.

1. Addressability in the tweezer array

The addressing laser pattern used to prepare the initial classical Néel configuration is generated by a 1013-nm laser beam detuned from the transition between the intermediate state $6P_{3/2}$ and $|\uparrow\rangle$ (Fig. 4b). The sign of the detuning sets the one of the light-shift: in the FM (resp. AFM) case, the frequency of the addressing laser is tuned below (resp. above) the resonance by ~ 250 MHz.

We use a dedicated spatial light modulator to produce the pattern of addressing beams. Each beam is focused on a $1/e^2$ radius of about $1.5 \mu\text{m}$, for a typical power of 60 mW. We measure the light-shift for each addressed atom by microwave spectroscopy on the $|\uparrow\rangle - |\downarrow\rangle$ transition. The average light-shift is $|\delta_0| = 2\pi \times 15$ MHz over the 42-atom array (21 addressed atoms), and $|\delta_0| = 2\pi \times 9$ MHz over the 100-atom array (50 addressed atoms). These values are dictated by available laser power. For both arrays, the rms dispersion of δ_0 across the addressing beams is 2.4%.

2. Experimental sequence

The experimental sequence is shown in Fig. 4. After assembling the array [52] we use Raman sideband cooling along the radial directions of the tweezers, and reach a temperature of $10 \mu\text{K}$. We then optically pump the atoms in $|g\rangle = |5S_{1/2}, F = 2, m_F = 2\rangle$ before adiabatically ramping down the tweezer depth by a factor ~ 40 . Following this, we switch off the tweezers, and excite the atoms to $|\uparrow\rangle$ using a two-photon stimulated Raman adiabatic passage (STIRAP) with 421-nm and 1013-nm lasers ($\sim 2 \mu\text{s}$ duration).

To generate the classical Néel configuration along z , we first transfer all the atoms from $|\uparrow\rangle$ to $|\downarrow\rangle$ using a 54 ns microwave π -pulse. Subsequently, the addressing beams are applied to the atoms in sublattice B. We then transfer the atoms A from $|\downarrow\rangle$ back to $|\uparrow\rangle$ by an adiabatic microwave sweep while the atoms B remain in $|\downarrow\rangle$, as illustrated in Fig. 4b. In this procedure, exciting first the atoms in $|\downarrow\rangle$ has the advantage of minimizing the depumping of the $|\uparrow\rangle$ atoms by the addressing light (see Sec. B 2 below). An example of perfect Néel configuration obtained at the end of the preparation is shown in Fig. 4c.

3. State detection procedure

At the end of the sequence, we read out the state of each atom in the natural z -basis. To do so, we deexcite the atoms from $|\uparrow\rangle$ to the $5S_{1/2}$ manifold where they are recaptured in the tweezers and imaged. Thus, the $|\uparrow\rangle$ (resp. $|\downarrow\rangle$) state is mapped to the presence (resp. absence) of the corresponding atom. In order to avoid the detrimental effects of the $|\uparrow\rangle - |\downarrow\rangle$ interaction-induced dynamics during the deexcitation, we freeze out the system by shelving the $|\downarrow\rangle$ atoms to $|D\rangle = |59D_{3/2}, m_j = -1/2\rangle$ where they hardly interact with the ones in $|\uparrow\rangle$. This is achieved by using a 48 ns microwave π -pulse at 10.6 GHz. The subsequent deexcitation is performed by applying a $2.5 \mu\text{s}$ light pulse resonant with the transition between $|\uparrow\rangle$ and the short-lived intermediate state $6P_{3/2}$ from which the atoms decay back to $5S_{1/2}$. Additionally, when we want to measure the spins along x we rotate them by applying a 27 ns microwave $\pi/2$ -pulse on the $|\uparrow\rangle - |\downarrow\rangle$ transition prior to the detection. However, this procedure is efficient only for light-shifts $|\delta(t)|$ much smaller than the microwave Rabi frequency, i.e. for times larger than $\sim 0.5 \mu\text{s}$ during an adiabatic preparation.

B. Experimental imperfections

The sequences described above are affected by experimental imperfections. As taking all of them into account is intractable, we estimate here the effect of the main imperfections on the quantities we measure. We first analyse the state preparation and measurement (SPAM) errors and then discuss decoherence in the system.

1. SPAM errors

In order to estimate the SPAM errors, we break down the sequence into a series of steps i , each having a small but finite failure probability η_i . In the following, we keep only the contributions of imperfections to first order in the η_i 's.

As an example, we show in Fig. 5 the discretized sequence corresponding to the preparation and measurement of the classical Néel configuration (corresponding to the time $t = 0$ in Fig. 2a of the main text). Table I gives the corresponding values of the probabilities η_i for 42 atoms, that are either inferred from a series of dedicated experiments, or estimated from numerical simulations. The table also mentions the physical origin of these imperfections.

For atoms in sublattice A (non-addressed), the error tree leads to the probability to recapture the atoms at the end of the sequence, which reads (to first order):

$$P_z^A \approx 1 - \eta_{\text{MW}} - \eta_A - \eta_{\text{dx}} - \epsilon. \quad (2)$$

Similarly, the calculation for sublattice B (addressed atoms) yields:

$$P_z^B \approx \eta_{\text{STIRAP}} + \eta_B + \epsilon'. \quad (3)$$

Stage	Step	Symbol	Value	Main physical origin
Classical Néel state preparation	Rydberg excitation	η_{STIRAP}	5%	Imperfect optical pumping, Laser phase noise, Spontaneous emission from $6P_{3/2}$ [53]
	MW π - pulse	η_{MW}	< 2%	Effect of H_{XY} during pulse
	MW sweep	η_A, η_B	6%, 3%	Effect of H_{XY} and finite value of $ \delta_0 $
Readout	Freezing	η_{frz}	< 1%	Effect of H_{XY} during pulse
	Deexcitation	η_{dx}	3%	Mechanical effect of deexcitation laser beam
	False positive	ϵ	1%	Background gas collisions [53]
	False negative	ϵ'	7%	Rydberg state radiative lifetime [53]

Table I. Summary of the experimental errors defined in Fig. 5, together with their main physical origin.

zations for the 10×10 arrays. In Fig. 2a, one observes that, in the FM case, the z -magnetizations of sublattices A and B do not vanish at late times, but reach a constant finite value of a few percent. In contrast, this does not occur in the AFM case (Fig. 2d). We qualitatively explain this effect by the following observations. First, due to off-resonant scattering by the addressing beam, atoms in $|\uparrow\rangle$ are slowly depumped to the ground state $|g\rangle$; we have measured the effective lifetime of an addressed $|\uparrow\rangle$ atom to be $\sim 4 \mu\text{s}$, whether the light-shift is $2\pi \times 15$ or $-2\pi \times 15$ MHz (so that this alone, cannot explain the difference between the FM and AFM cases). However, during our adiabatic ramp down of light-shift $\delta(t)$, the addressed atoms are initially in $|\downarrow\rangle$ (and thus cannot be depumped). Depumping sets in only when the system enters the ordered phase, where an addressed atom has a significant probability to be in $|\uparrow\rangle$. Since $\delta_c^{\text{AFM}} < \delta_c^{\text{FM}}$, the addressing beam intensity (and thus the depumping rate) is at this stage much smaller for the AFM case than for the FM case, and thus has a negligible effect in the former case.

Second, we investigate the role of decoherence on the appearance of long-range order along x in the FM case, for the 10×10 array. Figure 6a shows the time evolution of the nearest-neighbour correlations as we ramp down the light-shift, all the way up to $8 \mu\text{s}$ (in contrast with Fig. 2b of the main text where the evolution is shown only up to $3 \mu\text{s}$, and for 42 atoms). Two timescales appear: first, correlations build up until $t \simeq 1 \mu\text{s}$ as the FM state is adiabatically prepared; then, they slowly decay and lose 25 % of their value in $7 \mu\text{s}$. This decay is not expected, since the system should be ideally in steady state once it has reached the ferromagnetic phase. We conjecture that the experimental system is affected by decoherence arising from a combination of the residual atomic motion and spontaneous emission from the Rydberg states.

To further analyse the evolution of the ferromagnetic order, we probe the full spatial structure of the correlations at different times. Figure 6b summarizes the results. We observe that for a given distance d all the correlations feature a similar time evolution: a fast increase followed by a slow decay, with a turning point around $1 \mu\text{s}$. For this particular point, the data reveal a plateau for distances of more than 6 sites – the signa-

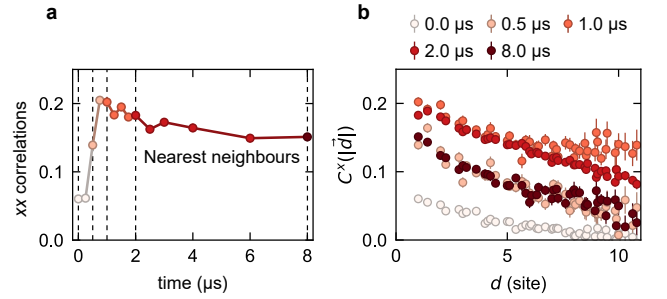


Figure 6. **Time dependence of the correlations along x in the FM case for a 10×10 lattice.** **a**, Time evolution of the nearest-neighbour correlations along x (different colors correspond to different times). **b**, Spatial correlations as a function of distance, measured at different times $t = \{0.0, 0.5, 1.0, 2.0, 8.0\} \mu\text{s}$ indicated by dashed lines in **a**.

ture of the long range order mentioned in the main text – that disappears for $t \gtrsim 2 \mu\text{s}$. This suggests that despite the decoherence present in the system, we are able to observe the long range ordering expected from the dipolar interactions over a substantial time window.

C. Determination of the crossover position in the phase diagram

We discuss here the position of the boundaries in the phase diagrams depicted in Fig. 1e,f. In order to identify this location, we fit each vertical column of the phase diagrams using an error function. We have chosen this simple functional form as it allows a relatively good match with the data (see black lines in Fig. 7). The position of the boundaries for the FM phase (resp. AFM) is then set by the value of δ_q at which the fit reaches an arbitrary threshold (depicted by the black triangle) of $m_{\text{FM}}^2 = 0.127$ (resp. $m_{\text{AFM}}^2 = 0.05$). This threshold is approximately halfway between the maximum and minimum values of m_{FM}^2 (resp. m_{AFM}^2) measured across the phase diagram. The vertical and horizontal error bars in Fig. 1e,f are

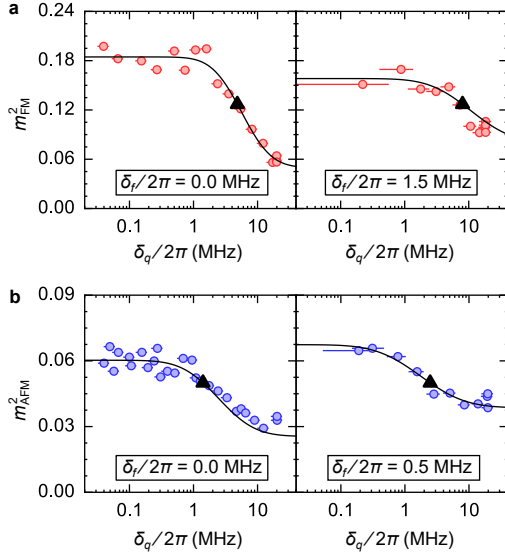


Figure 7. **Determination of the phase diagrams boundaries.** Order parameter m^2 as a function of the quench light-shift δ_q for various final light-shifts δ_f , in the FM case (a) and in the AFM case (b). The experimental points are fitted with an error function (black line) as explained in the text. Black triangles locate the positions of the boundaries.

dominated by the uncertainties on the calibrations of δ_q and δ_f (due to the combined effect of power drifts and systematic errors, we estimate the uncertainty to be around 15%).

D. Ground state properties of the XY model

We study here the ground states of the Hamiltonians H_{XY} and $H_{XY} + H_Z$. We define them as in the main text. First:

$$H_{XY} = -\frac{J}{2} \sum_{i < j} \frac{a^3}{r_{ij}^3} [\sigma_i^x \sigma_j^x + \sigma_i^y \sigma_j^y] \quad (4)$$

$$= -\frac{J}{\hbar^2} \sum_{i < j} \frac{a^3}{r_{ij}^3} [S_i^+ S_j^- + S_j^+ S_i^-] \quad (5)$$

where $S_i^\pm = S_i^x \pm i S_i^y = \hbar(\sigma_i^x \pm i \sigma_i^y)/2$ are the ladder operators for spin-1/2 degrees of freedom on a square lattice with N sites, r_{ij} is the distance between sites i, j and a is the lattice spacing. Second, the on-site Hamiltonian is:

$$H_Z = \hbar \delta \sum_{i \in B} \frac{\sigma_i^z + 1}{2} \quad (6)$$

where the magnitude of the light-shift δ depends on the intensity of the addressing laser.

The experimental implementation has a ferromagnetic coupling, $J/\hbar = 0.77$ MHz, and to study antiferromagnetism one must prepare negative temperature states. For theoretical purposes, however, we treat J as a free parameter and frame the discussion in terms of the ground state physics of H_{XY} with either ferromagnetic ($J > 0$) or antiferromagnetic ($J < 0$) coupling. We refer to them as H_{XY}^{FM} and H_{XY}^{AFM} .

It is natural to compare the dipolar H_{XY} to the nearest-neighbor XY model on the square lattice,

$$H_{\text{nn}} = -\frac{J}{2} \sum_{\langle ij \rangle} \sigma_i^x \sigma_j^x + \sigma_i^y \sigma_j^y, \quad (7)$$

where $\langle ij \rangle$ are pairs of neighboring sites, with $i < j$. For H_{nn} , the sign of the coupling J is unimportant, as $U_A H_{\text{nn}} U_A^\dagger = -H_{\text{nn}}$, with $U_A = \prod_{j \in A} e^{-i\pi S_j^z}$. In 1988, Kennedy, Lieb, and Shastry rigorously proved that the unique ground state of H_{nn} has long-range XY order (LRO) [54].

For models with long-range interactions, there are analogous mathematical theorems for classical systems at finite temperature, and for quantum systems in which the interaction strength depends on the Manhattan distance $\|r_i - r_j\|_1$ [25]. In a recent work, Björnberg and Ueltschi addressed quantum spin- S models with interactions depending on the Euclidean distance $\|r_i - r_j\|_2$, although their results require large S and spatial dimension three or higher [55]. Absent a rigorous proof of LRO for the two-dimensional, spin-1/2, dipolar XY model, one can study it using semi-analytic spin wave theory and various numerical methods [24, 28, 31]. In a companion paper [56], we investigate the ground-states of H_{XY} on various geometries, such as tori and infinite cylinders, with an eye towards the thermodynamic limit, $N \rightarrow \infty$. Here, we restrict our focus to finite rectangular arrays as probed in the experiment, and use H_{nn} as a reliable benchmark for comparison.

1. Symmetries, magnetization sectors, and order

As emphasized in the main text, H_{XY} possesses the continuous symmetry: $U_z(\theta) H_{XY} U_z(-\theta) = H_{XY}$ with

$$U_z(\theta) = \exp(-i \sum_j \theta S_j^z / \hbar) = \exp(-i \theta M^z / 2) \quad (8)$$

This operator is generated by the total magnetization, $M^z = \sum_i \sigma_i^z$, and represents the Lie group $U(1) \cong SO(2)$. Additionally, H_{XY} is invariant under the \mathbb{Z}_2 Ising symmetry, $\alpha_2 : (\sigma^x, \sigma^y, \sigma^z) \rightarrow (\sigma^x, -\sigma^y, -\sigma^z)$, as well as any spatial symmetries of the lattice, such as translation or rotation. This model is also time-reversal-symmetric, as represented by the anti-unitary operator $\mathcal{T} = \mathcal{C}$, where \mathcal{C} applies complex conjugation. Here \mathcal{T} differs from the usual $SU(2)$ time-reversal symmetry, which applies the unitary spin rotation $U_y(\pi) = \exp(-i\pi M^y/2)$ in addition to \mathcal{C} . Our atypical choice of $\mathcal{T} = \mathcal{C}$ allows it to remain a symmetry in the presence of the on-site perturbation, H_Z .

In a finite, closed quantum system, all eigenstates $|\psi_n\rangle$ of H_{XY} can be chosen to be simultaneous eigenstates of all of these symmetry operators. In particular, they are eigenstates of the total magnetization, $M^z |\psi_n\rangle = \lambda_n^z |\psi_n\rangle$, and so can be collected into magnetization sectors, conventionally labeled by $S^z = M^z/2$. As a consequence, all M^z -non-conserving operators such as σ_i^x and σ_i^y have identically vanishing expectation values, $\langle \sigma_i^x \rangle = \langle \sigma_i^y \rangle = 0$, in any energy eigenstate $|\psi_n\rangle$, or in any superposition of eigenstates within the same magnetization sector.

In the experiment, systematic errors in the measurement process lead to a small, nonzero $\langle \sigma_i^x \rangle \neq 0$. This value is not a consequence of the physics we are interested in. When analyzing the experimental data, we thus choose to nullify any single-spin contributions by using the *connected* correlator,

$$C^x(i, j) = \langle \sigma_i^x \sigma_j^x \rangle - \langle \sigma_i^x \rangle \langle \sigma_j^x \rangle \quad (9)$$

In the special case of M^z eigenstates with $\langle \sigma^x \rangle = 0$, $C^x(i, j) = \langle \sigma_i^x \sigma_j^x \rangle$. This correlation function is not generically zero. If $|C^x(i, j)|$ approaches a constant $m_0^x > 0$ for distantly separated spins i, j , then the corresponding state is said to possess *long-range XY order* or *off-diagonal long-range order* (LRO) [12]. Such LRO is the defining feature of continuous symmetry breaking in finite quantum systems.

Rather than the long-distance plateau, an equally good order parameter for $U(1)$ symmetry breaking is given by the in-plane magnetization squared

$$m_{\text{FM/AFM}}^2 = \frac{1}{N^2} \sum_{i,j} (\pm 1)^{(r_i^x + r_j^y)/a} C^x(i, j) \quad (10)$$

where a is the lattice spacing, and the sign is taken $+1$ for m_{FM}^2 , and -1 for m_{AFM}^2 . In the thermodynamic limit, $N \rightarrow \infty$, any state with a correlation plateau $m_0^x \neq 0$ will also have a finite magnetization $m_{\text{FM/AFM}}^2$, and vice versa [50].

2. DMRG calculations

For the numerical investigation of the ground states, we apply the density matrix renormalization group (DMRG) algorithm [48]. We employ the general matrix product state (MPS) framework implemented in the TeNPy software library [49]. While MPS are best-representative of one-dimensional quantum systems, it is now routine to apply DMRG to two-dimensional models under certain geometric restrictions [57]. We always work with charge-conserving tensors that respect the $U(1)$ symmetry of the Hamiltonian.

To begin, we use DMRG to compute the ground state of H_{XY} and H_{nn} on $L \times L$ square clusters with open boundary conditions, for $L = 4, 6, 8$, and 10 . With all-to-all interactions included, we reliably obtain well-converged states at relatively low MPS bond dimensions, χ , as quantified by the truncation error of the discarded Schmidt states, ϵ_{trunc} . The most difficult finite system we study is $H_{\text{XY}}^{\text{AFM}}$ on the 10×10 lattice, for which $\epsilon_{\text{trunc}} < 10^{-5}$ at $\chi = 2048$. All other cases achieve the same or better convergence by $\chi = 1024$, or even $\chi < 200$ on the smaller systems.

All DMRG ground states feature the strong $\langle \sigma^x \sigma^x \rangle$ correlations expected in an XY LRO state. In Fig. 8a, we show the real-space correlation profile $C^x(d)$, which averages $C^x(i, j) = \langle \sigma_i^x \sigma_j^x \rangle$ over all spins i, j separated by a displacement vector \vec{d}_{ij} with length d . The long-range-interacting ferromagnet, $H_{\text{XY}}^{\text{FM}}$, exhibits a clear plateau in $C^x(d)$ at long distances for all system sizes. Such a plateau is less apparent for $H_{\text{XY}}^{\text{AFM}}$ and H_{nn} , although for either model $C^x(d)$ is still quite large at the longest distances. Furthermore, $C^x(d)$ increases

with L in both models, suggesting the spatial decay of $C^x(d)$ is amplified by finite-size effects.

We also look for a finite squared magnetization, $m_{\text{FM/AFM}}^2$. We plot the finite-size dependence of this quantity in Fig. 8b, which is consistent with $m_{\text{FM/AFM}}^2 > 0$ as $L \rightarrow \infty$. To further test the effects of the long-range interactions, we introduce a cutoff radius R_{max} , and only include interactions between spins i, j separated by distance $d_{ij} < R_{\text{max}}$. We find that ground state properties converge quickly with respect to this approximation parameter; the long-range interactions do not induce a quantum phase transition in either model. In Fig. 8c, we show the dependence of $m_{\text{FM/AFM}}^2$ on R_{max} , finding that, at fixed system size, it is not strongly dependent on $R_{\text{max}} > 4$. This is not too surprising: with the moderately fast $1/r^3$ decay, the interaction strength beyond this point is on the order of $0.01 J$ or less.

Overall, $H_{\text{XY}}^{\text{FM}}$ is clearly XY LRO, while $H_{\text{XY}}^{\text{AFM}}$ and H_{nn} exhibit stronger finite-size effects. Given that H_{nn} is rigorously known to be LRO in the thermodynamic limit, the similar behavior observed for $H_{\text{XY}}^{\text{AFM}}$ is a strong indication that it is as well.

3. Quantum phase diagram of $H_{\text{XY}} + H_Z$

We now investigate the ground state phase diagram in the presence of the externally applied light-shift δ , described by H_Z (Eq. 6). This perturbation preserves the $U(1)$ symmetry of H_{XY} , as well as the anti-unitary time-reversal symmetry. On the other hand, H_Z breaks the Ising symmetry $\sigma_i^z \rightarrow -\sigma_i^z$, and reduces the spatial rotation and translation symmetries. For sufficiently large δ , the lowest energy state of $H_{\text{XY}} + H_Z$ has $M^z \neq 0$, but such states are dynamically decoupled from the $S^z = 0$ sector in which the adiabatic preparation protocol takes place. Henceforth, we always consider the ground states within the $S^z = 0$ sector, as these are the ones most relevant to the experiment.

Because the perturbation H_Z is $U(1)$ symmetric, the XY LRO phase of H_{XY} may be stable to a sufficiently small staggered field. Microscopically, the dominant effect of a small δ should be to slightly cant the spins towards the z -axis. This will in turn modify the spin stiffness and the spin wave velocity, but not destroy the underlying order. By contrast, when δ is very large, the ground state must be a gapped, trivial paramagnet, in which $\langle \sigma^x \sigma^x \rangle$ correlations decay to zero at long distances [58]. Between these two limits, we expect a quantum phase transition (QPT) at some critical value, δ_c , of the applied field. In a companion paper [56], we investigate this QPT in detail, finding that, in the thermodynamic limit, it is likely a continuous, second-order transition. For $H_{\text{nn}} + H_Z$, the transition is in the 3D XY universality class.

Here, we focus our attention on the 6×7 and 10×10 arrays studied in the experiment. We calculate the $S^z = 0$ ground state of $H_{\text{XY}} + H_Z$ at various light-shifts δ using DMRG. At these system sizes, the sharp QPT expected in the thermodynamic limit is smoothed to a broad crossover between the XY-ordered phase for small δ , and a trivial paramagnet for large δ . Three features of this crossover are shown in Fig. 8d-f.

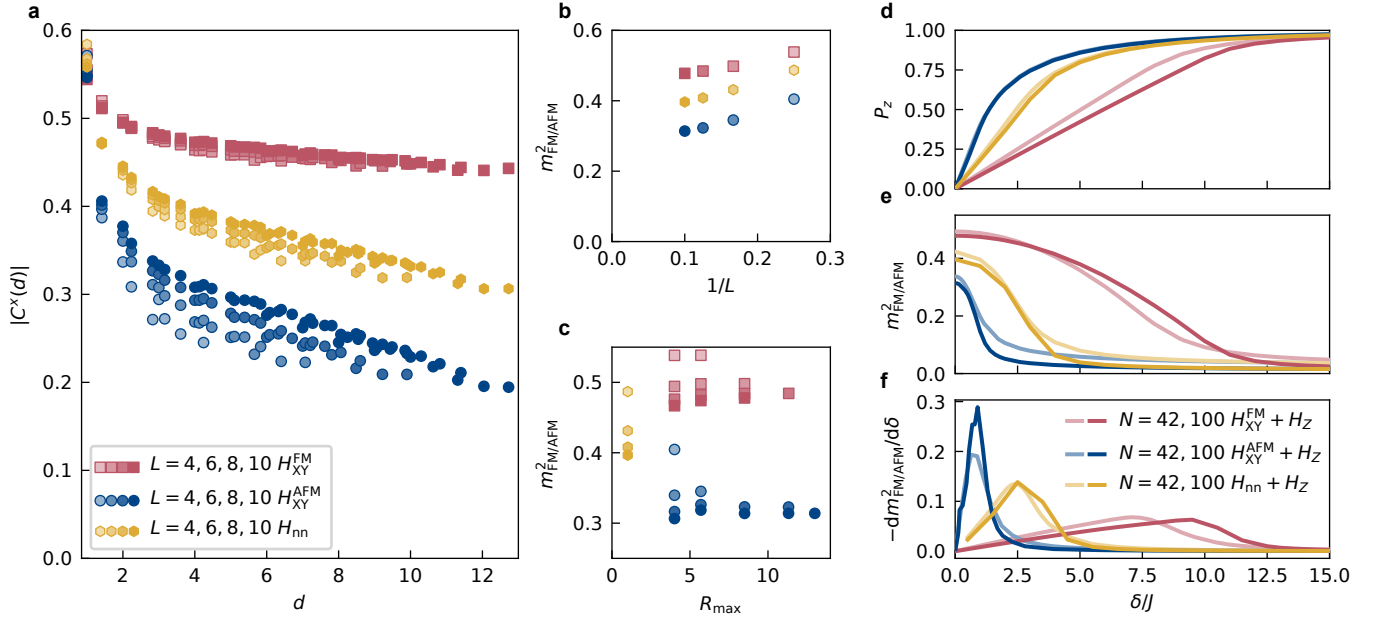


Figure 8. **DMRG ground state calculations.** **a**, Real-space correlation profile $|C^x(d)|$ on $L \times L$ square clusters with open boundary conditions. The ground state of H_{XY}^{FM} clearly exhibits XY LRO at all system sizes. For H_{XY}^{AFM} and H_{nn} , the correlations decrease at long distances, but this decay is reduced as L increases. **b**, Finite-size scaling of the magnetization $m_{\text{FM/AFM}}^2$. All three models are consistent with $m_{\text{FM/AFM}}^2 > 0$ as $L \rightarrow \infty$. **c**, Dependence of $m_{\text{FM/AFM}}^2$ on the interaction distance cutoff R_{max} . At each system size, the ground state correlations are well-converged by $R_{\text{max}} \approx 4$. **d-f**, Ground state properties of $H_{XY} + H_Z$ as a function of δ . There is a smooth crossover from the XY ordered state at $\delta = 0$ to the staggered paramagnet as $\delta \rightarrow \infty$. The $-dm^2/d\delta$ peaks (**f**) are finite-size incarnations of the quantum phase transition expected in the thermodynamic limit; we use their centers to define the crossover point $\hbar\delta_c/J$.

First, in Fig. 8d, we plot the staggered σ^z polarization,

$$P_z = \frac{1}{N} \sum_{i \in A} \langle \sigma_i^z \rangle - \frac{1}{N} \sum_{i \in B} \langle \sigma_i^z \rangle \quad (11)$$

which measures the alignment with the staggered field H_Z . For large $\delta \gg \delta_c$, the ground state approaches the staggered product state used to initialize the adiabatic ramp in the experiment, and the polarization saturates to $P_z = 1$. For $\delta = 0$, $P_z = 0$ due to the Ising symmetry of H_{XY} , which enforces $\langle \sigma_i^z \rangle = 0$. We emphasize that $P_z = 0$ is *not* a generic feature of the XY-ordered phase. Indeed, for small $\delta < \delta_c$, the spins partially align with the applied field, yielding $P_z > 0$.

Figure 8e displays the complementary behavior for the magnetization, $m_{\text{FM/AFM}}^2$. At small δ , the field-induced canting of the spins towards the z -axis causes $m_{\text{FM/AFM}}^2$ to decrease proportionally to δ^2 . At large δ , the ground state approaches the (staggered) z -aligned product state, in which $m_{\text{FM/AFM}}^2 = 0$. The magnetization changes most rapidly at the crossover, giving rise to the clear peaks in $dm_{\text{FM/AFM}}^2/d\delta$ shown in Fig. 8f. We take the center of these peaks as our definition of the crossover point, $\delta_c^{\text{FM/AFM}}$. For the $N = 42$ cluster, the values are $\hbar\delta_c^{\text{FM}}/J = 7.1(3)$, $\hbar\delta_c^{\text{AFM}}/J = 0.8(1)$, and $\hbar\delta_c^{\text{nn}}/J = 2.4(1)$. For the $N = 100$ cluster, we find $\hbar\delta_c^{\text{FM}}/J = 9.5(3)$, $\hbar\delta_c^{\text{AFM}}/J = 0.9(1)$, and $\hbar\delta_c^{\text{nn}}/J = 2.5(9)$. As $N \rightarrow \infty$, the smooth crossover is expected to sharpen into a *bona fide* QPT, and $m_{\text{FM/AFM}}^2(\delta)$ will be non-analytic at the critical point.

E. Adiabatic preparation - theory and numerics

We now provide theoretical and numerical analyses of the adiabatic preparation protocol used in the experiment. As mentioned above, we study both the FM and AFM cases considering $H_{XY}^{\text{AFM}} = -H_{XY}^{\text{FM}}$. Additionally, for a time-reversal-symmetric Hamiltonian such as $H = H_{XY} + H_Z$, the dynamics under $H(t)$ and $-H(t)$ are identical (as long as the initial state is also time-reversal-symmetric) [45]. So for a finite-time (quasi-adiabatic) ramp, the diabatic errors incurred attempting to follow the topmost state of $H_{XY}^{\text{FM}} + H_Z$ are the same as for a ground-state protocol with $H(t) = H_{XY}^{\text{AFM}} - H_Z(t)$.

1. Excitation gaps and an alternative protocol

The success of any finite-duration adiabatic protocol depends crucially on the low-energy spectrum of the system. In particular, as the smallest excitation gap encountered along the chosen path through parameter space decreases, the time required to obtain a final, high-fidelity ground state increases. To this end, we computed the minimal energy gaps, Δ_{min} , using exact diagonalization on finite clusters with periodic boundary conditions.

In Fig. 9a, we plot the instantaneous gap Δ_{min} of $H_{XY}^{\text{FM/AFM}} + H_Z$, in the $S^z = 0$ sector, as a function of the light-shift $\hbar\delta/J$. We expect the gap for either case to be small-

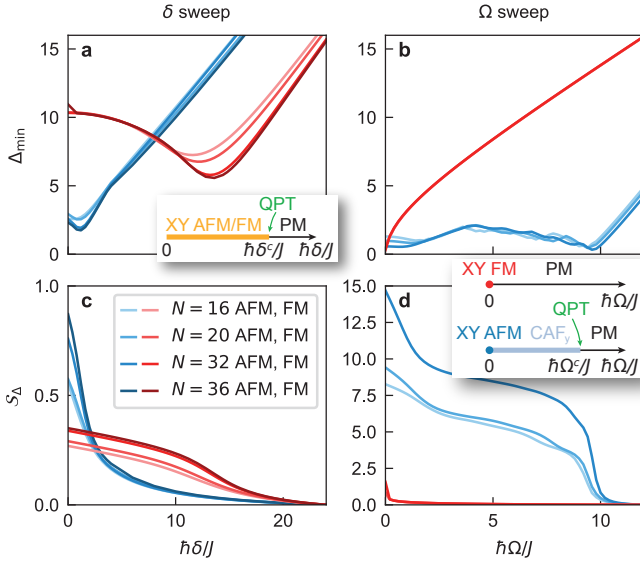


Figure 9. **Excitation gap for two adiabatic preparation protocols.**

a. Minimal energy gaps of $H_{XY}^{\text{AFM(FM)}} + H_Z$ to the lowest excited state in the $M^z = 0$ sector as a function of $h\delta/J$. We here only consider gaps among states with momentum $\vec{k} = 0$ and fully symmetric under the lattice point-group, which reflects the setup in the (ideal) experiment. Blue (red) curves show the results for the AFM (FM) model. Darker colors correspond to larger system sizes. The inset shows a sketch of the expected phase diagram. **b.** Same as **a**, but for the protocol with Hamiltonian $H_{XY}^{\text{AFM(FM)}} + H_X$. Here we cannot restrict the analysis to a single M^z sector since it is not conserved. **c.** Cumulatively integrated $1/\Delta_{\min}^2$ [starting from the largest value $h\delta/J = 24$] for the gaps shown in **a**. The values at $h\delta/J = 0$ measure how difficult it is to prepare the ground state of $H_{XY}^{\text{AFM(FM)}}$ by sweeping δ . **d.** Same as **c** but for the gaps along Ω , as shown in **b**. The inset shows a sketch of the expected phase diagrams for $H_{XY}^{\text{AFM(FM)}} + H_X$.

est near the quantum phase transition (Methods D3): for the FM, this dip is seen at $h\delta/J \approx 12$, while in the AFM the gap is minimal when $h\delta/J \lesssim 2$. The size of the minimal gaps decreases with increasing system size N (darker colors), as one would expect at a QPT. However, we find the minimal finite-size gaps for the FM model are always larger than the ones for the AFM model. This indicates that for the dipolar XY model, the FM requires less total ramp time to prepare than the AFM.

Besides the staggered light-shift ramp demonstrated in the main text, one can conceive a different route for preparing XY-ordered states: tune down a spatially *uniform* field in the x direction from large values $h\Omega \gg J$ to zero. This is similar to what is done in Rydberg quantum simulations of the two-dimensional Ising model [8, 9, 59], and was used in a prior experiment to prepare the topological ground state of a one-dimensional XY model [60]. The corresponding Hamiltonian is $H_{XY}^{\text{AFM(FM)}} + H_X(t)$, with $H_X(t) = \hbar\Omega(t) \sum_i \sigma_i^x/2$. Note that M^z is no longer conserved in the presence of H_X .

Figure 9b shows the smallest energy gap for this alternative protocol. The behaviour is very different from the one for the δ sweep discussed above. For FM interactions, the

gap does not show any local minimum and remains large until the end of the sweep, where it finally narrows. By contrast, the gap for the XY AFM is small in the whole region $h\Omega/J \lesssim 10$. Based on previous studies of the nearest-neighbor XY model [61, 62], both of these results are likely a consequence of the expected phase diagram for $H_{XY}^{\text{FM/AFM}} + H_X$, which we sketch in the inset of Fig. 9d. For the XY FM, H_X is a relevant perturbation to the ordered phase: any non-zero Ω breaks the $U(1)$ symmetry and, in the thermodynamic limit, immediately destroys the LRO, resulting in a paramagnetic (PM) phase. The AFM is also XY-ordered only at the $U(1)$ -symmetric point $\Omega = 0$, but a small Ω instead “cants” the AFM order towards the y -direction by a spin-flop process [61, 62]. The ground state is then still an antiferromagnet, but one ordered along the y -direction, i.e. it spontaneously breaks the remaining \mathbb{Z}_2 symmetry $\sigma^y \rightarrow -\sigma^y$ of $H_{XY} + H_X$. This “canted” antiferromagnet (CAF_y) is stable up to a critical value $h\Omega_c/J$ where it finally undergoes a 2 + 1D Ising QPT to the PM phase [62].

Comparing the gap landscapes in Fig. 9a,b suggests that preparing the XY AFM requires less time when using δ sweeps instead of the Ω sweeps. To quantify this, we integrate the squared inverse gaps and define

$$\mathcal{S}_\Delta(\lambda) = \int_{\lambda_0}^{\lambda} \frac{1}{\Delta_{\min}(\lambda')^2} d\lambda' \quad (12)$$

where $\lambda = h\delta/J$ or $h\Omega/J$ is the dimensionless parameter for either protocol. As one motivation for this quantity, we consider the fidelity susceptibility, χ_F , which is the leading term in the expansion of the fidelity $F(\lambda, \lambda + \delta\lambda) = |\langle \psi_0(\lambda) | \psi_0(\lambda + \delta\lambda) \rangle|$ of the ground states $|\psi_0(\lambda)\rangle$ between two close points λ and $\lambda + \delta\lambda$ in parameter space [63],

$$F(\lambda + \delta\lambda) = 1 - \frac{\delta\lambda^2}{2} \chi_F + \dots \quad (13)$$

The coefficient χ_F characterizes how quickly the ground state changes with λ . For a ramp protocol of the form $H(\lambda) = H_{XY} + \lambda H_I$, one can show

$$\chi_F = \sum_{n \neq 0} \frac{|\langle \psi_n(\lambda) | H_I | \psi_0(\lambda) \rangle|^2}{(E_n(\lambda) - E_0(\lambda))^2} \quad (14)$$

where $|\psi_n(\lambda)\rangle$ is the n -th eigenstate of $H(\lambda)$ and $E_n(\lambda)$ is the corresponding energy [63]. If we assume that the $n = 1$ term is dominant, and the numerator is nearly constant, we get the relationship $\chi_F \sim 1/(E_1(\lambda) - E_0(\lambda))^2 = 1/\Delta_{\min}(\lambda)^2$. The integral \mathcal{S}_Δ therefore estimates the total difficulty of adiabatically preparing the ground state of $H(\lambda)$, starting from the ground state of $H(\lambda_0)$.

In Fig. 9c,d, we plot $\mathcal{S}_\Delta(\lambda)$ for the two protocols. The initial point λ_0 is taken to be in the paramagnetic phase: $\lambda_0 = 12$ for the δ sweep and $\lambda_0 = 24$ for the Ω sweep. In either case, \mathcal{S}_Δ for the AFM (blue curve) exceeds that of the FM as $\lambda \rightarrow 0$, indicating that the AFM is more difficult to prepare. Most importantly, comparing Fig. 9c,d, one sees that the $H_Z(t)$ protocol is much more efficient at preparing the XY ordered state ($\lambda = 0$) than the $H_X(t)$ protocol, especially for the AFM.

2. Time-dependent MPO-MPS simulation

To ensure that we have a good understanding of the experiment and its imperfections, we also perform numerical simulations of the full many-body quantum dynamics for the $N = 42$ adiabatic ramp. We simulate the dynamics in the spin-1/2 subspace, taking into account the error tree in Fig. 5 by sampling the state preparation errors with $N_{\text{dis}} = 20$ independent simulations.

Atoms that were not excited in the STIRAP with $\eta_{\text{STIRAP}} = 0.03$ correspond to missing sites in the square lattice not taking part in the dynamics. On the remaining sites, we prepare an initial MPS as product state, flipping individual spins according to the probabilities of the microwave π -pulse, $\eta_{\text{MW}} = 0.003$, and the subsequent microwave sweep of the addressed atoms, $\eta_{\text{A}} = 0.10$, $\eta_{\text{B}} = 0.03$. These values are slightly different from those reported in Table I, reflecting an earlier calibration of the experiment. We further update the atom distances r_{ij} in H_{XY} to account for positional disorder: we first take a normal-distributed initial displacement from the square lattice with variance $\sigma_r = 0.2 \mu\text{m}$, followed by a movement during the dynamics with normal-distributed (time-independent) velocity of variance $\sigma_v = 0.05 \mu\text{m}/\mu\text{s}$ corresponding to the temperature of the atoms.

We then time-evolve the states under the time-dependent Hamiltonian,

$$H(t) = -J \sum_{i < j} \frac{a^3}{r_{ij}^3(t)} [S_i^+ S_j^- + S_i^- S_j^+] + H_{\text{vdW}} + \delta(t) \epsilon_{\text{AFM}} \sum_{i \in B} \frac{1 + \sigma_i^z}{2} \quad (15)$$

where $J/h = 0.77 \text{ MHz}$, $\delta(t)$ is the ramp shown in Fig. 10a,c (insets), and $\epsilon_{\text{AFM}} = -1$ for the antiferromagnet (+1 for the ferromagnet). The additional term, H_{vdW} , accounts for the van der Waals interactions between the Rydberg atoms, and takes the form

$$H_{\text{vdW}} = \sum_{i < j} \frac{a^6}{r_{ij}^6(t)} [U_6^{PP} P_i^\uparrow P_j^\uparrow + U_6^{SS} P_i^\downarrow P_j^\downarrow + U_6^{SP} (P_i^\uparrow P_j^\downarrow + P_i^\downarrow P_j^\uparrow)] \quad (16)$$

where $P_i^{\uparrow/\downarrow} = S_i^z \pm 1/2$ are single-spin projectors. The values of the U_6 coefficients are $U_6^{PP}/h = -0.008 \text{ MHz}$, $U_6^{SS}/h = 0.037 \text{ MHz}$, and $U_6^{SP}/h = -0.0007 \text{ MHz}$. For the purposes of this simulation, we restrict the interaction range of H_{XY} and H_{vdW} to $R_{\text{max}} < 3.7$. We use the W_{II} method [64] to approximate the evolution operator $e^{-i(H/h)dt}$ as a matrix product operator (MPO), in combination with standard variational MPO-MPS compression methods. Our scheme is correct to first order in the time step $dt = 0.01 \mu\text{s}/2\pi$. Since the evolution is sufficiently adiabatic, a moderate bond dimension of $\chi = 128$ is enough to capture the correlations. In the DMRG ground state, the truncation error at this bond dimension is 6×10^{-7} for the ferromagnet, and 3×10^{-5} for the antiferromagnet.

When evaluating expectation values and correlation functions from the time-evolved MPS (t -MPS), we further account for the measurement errors $\eta_{\text{frz}} = 0.01$, $\eta_{\text{dx}} = 0.03$, $\epsilon = 0.01$, $\epsilon' = 0.07$ of the error tree. This can be done exactly (without another sampling procedure), since the MPS gives full access to the probabilities of the individual measurement outcomes.

There are two notable experimental imperfections that we do not take into account in these simulations. First, there are further sources of decoherence in the experiment as discussed in B 2. Second, in our numerical simulations, we assume that all errors in the error tree occur independently for each atom and result in an initial product state of up or down spins or vacant holes. Yet, the STIRAP and microwave pulses leave the atoms in coherent superpositions of the relevant atom levels.

3. Simulation results for $N = 42$

The results of the t -MPS simulations are shown in Fig. 10, which also includes direct comparisons to the experimental measurements, and to the DMRG ground state. For our ensemble of $N_{\text{dis}} = 20$ independent t -MPS simulations, we show the average values of these simulations with solid lines, while the shaded region indicates the standard deviation.

Our first observable (Fig. 10a,c) is the staggered polarization $P_z = \sum (\pm)_{A,B} \langle \sigma_i^z \rangle$. For the antiferromagnet, the agreement between the t -MPS simulations and experiment is essentially perfect for all values of δ . This is a strong indication that most dominant sources of error in the experiment have been accurately accounted for. For the ferromagnet, there is a small offset between the t -MPS calculation and the experimental result at late times (small δ). In particular, $P_z \rightarrow 0$ as $\delta \rightarrow 0$ for the t -MPS calculation, while $P_z \rightarrow -0.06$ in the experiment. This discrepancy is due to the sublattice-dependent depumping from the light-shift discussed in Sec. B 2, which we do not account for in the t -MPS simulations.

As the state loses its initial σ^z polarization, it concomitantly develops XY order. This is tracked by the order parameter m_{FM}^2 (m_{AFM}^2 for the antiferromagnet), shown in Fig. 10b,d. We obtain again a good agreement between the t -MPS simulation and the experiment at early times (large δ), although we caution that the initial positive value of $m_{\text{FM/AFM}}^2 = 1/42$ is inherent to any σ_i^z -product state. On top of the smooth adiabatic envelope, the t -MPS simulations reveal coherent oscillations in P^z and $m_{\text{FM/AFM}}^2$. These oscillations are a feature of the large- δ paramagnetic phase, and are essentially Rabi oscillations between the classical Néel ground state and the 42-fold degenerate manifold of states with one spin-flip excitation.

At small δ , the experimental measurements of $m_{\text{FM/AFM}}^2$ fall below the t -MPS predictions. This deficit likely arises from a combination of decoherence and unmodeled systematic errors, such as experimental imperfections in the $\pi/2$ -pulse rotation to the x basis. Regarding the latter, an imperfect basis rotation means that the operator measured in the experiment is not exactly σ_i^x but some small modification of it, $\tilde{\sigma}_i^x = U \sigma_i^x U^\dagger$. In XY-ordered states, $\langle \sigma^x \sigma^x \rangle = \langle \sigma^y \sigma^y \rangle$ correlations are typically much larger than any other two-body

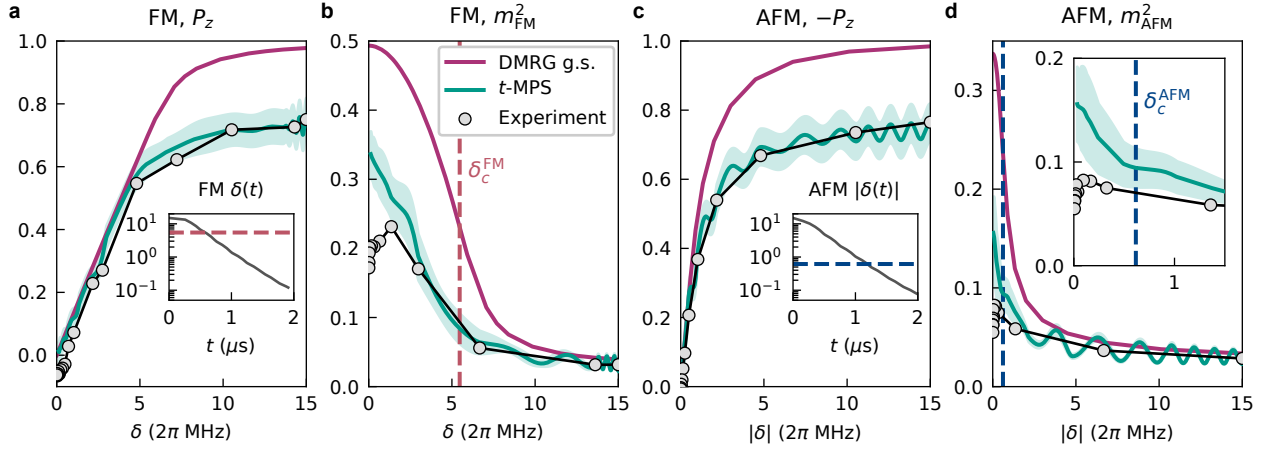


Figure 10. **Numerical simulation of the adiabatic preparation for the 6×7 lattice.** We compare the predictions from the t -MPS simulations (disorder ensemble average in dark teal, standard deviation in light teal) to the experimental data (gray), as measured at light-shift $\delta(t) = \delta$. We also show the ground-state expectation value from DMRG (purple) **a**, The staggered polarization P_z of the FM. Theory and experiment agree remarkably well, except for an offset at small δ , due to the light-shift-induced depumping. Inset: ramp $\delta(t)$ used for the FM simulation. **b**, The ferromagnetic magnetization $m_{\text{FM}}^2(\delta)$. We find excellent agreement between experiment and numerics for $\delta > 2$, including near the phase transition at $\delta_c^{\text{FM}} = 5.5$ (red dashed line). The two diverge somewhat at smaller δ (later times), likely due to decoherence and unmodeled systematic measurement errors. **c, d**, Corresponding results for the AFM. For P_z , the t -MPS simulation accurately reproduces the experimental data across the whole $\delta(t)$ sweep. For δ far above $\delta_c^{\text{AFM}} = 0.6$ (blue dashed line), there are many-body Rabi oscillations characteristic of the paramagnetic phase. **c**, Inset: ramp $\delta(t)$ used for the AFM simulation. **d**, Inset: zoom-in of lower left corner. At small δ (late times), the magnetization m_{AFM}^2 measured in experiment is below that predicted from the simulations.

operators, especially at long distances. Measuring any modified $\tilde{\sigma}_i^x$ will then generically reduce the value of the inferred magnetization, $\tilde{M}_{\text{FM}}^2 = 2 \sum_{i,j} \langle \tilde{\sigma}_i^x \tilde{\sigma}_j^x \rangle$.

We also use the t -MPS simulation to assess the quality of the adiabatic preparation. In particular, we are interested in how close the unitary dynamics comes to preparing the target ground state of H_{XY} . We measure this via the XY energy $E_{\text{XY}} = \langle H_{\text{XY}} \rangle$, which corresponds to the amount of energy the many-body state stores within the dipolar interaction. The ideal endpoint of the ramp is a state that minimizes E_{XY} , i.e. the ground state of H_{XY} (or, the topmost state in the case of the negative-temperature preparation for the antiferromagnet). We do not include measurement errors for this analysis, as we want to directly compare the adiabatically prepared state to the ideal one. As a minor technical point, the ensemble of lattices used in the t -MPS simulation occasionally have missing sites (representing an absence of Rydberg-excited atoms), and always have some position disorder which modifies the couplings, Ja^3/r_{ij}^3 , and hence the spectrum of H_{XY} . To treat the different lattices on even footing, when measuring E_{XY} we compute the expectation value of H_{XY} without position disorder in the couplings, and normalize by the total number of active sites, \bar{N} , before taking the ensemble average.

Figures 11a,b show $E_{\text{XY}}(\delta)/J\bar{N}$ in the DMRG ground state (purple), the ensemble-averaged t -MPS simulation (teal), and a single state within the t -MPS ensemble (pink) that had a nearly perfect initial configuration: one missing site at the corner, and all remaining spins properly aligned with the staggered field. Initially, the system is in a classical ensemble of σ_i^z -aligned product states, so $E_{\text{XY}}(t=0) = 0$. The dynamics generated by $H(t)$ produce the desired corre-

lations among the spins; the oscillations in E_{XY} at large δ are the paramagnetic Rabi oscillations also observed in P_z and m_x^2 . At the end of the ramp, the ensemble averages are $E_{\text{XY}}^{\text{FM}}/(\bar{N}J) = -1.41(8)$ and $E_{\text{XY}}^{\text{AFM}}/(\bar{N}J) = -0.64(3)$, which respectively correspond to $94 \pm 5\%$ and $89 \pm 4\%$ of the $N = 42$ ground state value. Remarkably, the near-ideal initial state produces a near-ideal final state, achieving 99.7% (FM) and 98.2% (AFM) of the ground state energy density. This indicates that any diabatic errors during the ramp are negligible compared to the initialization errors.

As discussed in Sec. E1, the quality of a finite-time adiabatic ramp crucially depends on the size of the many-body energy gap. For the $U(1)$ -symmetric ramp at hand, the quantity is the (spin-)neutral gap, $\Delta_0 = E_1(S^z = 0) - E_0(S^z = 0)$. In the paramagnetic phase, $\Delta_0 \sim \delta$, while in the XY-ordered phase one expects $\Delta_0^{\text{FM}} \sim 1/\sqrt{N}$ and $\Delta_0^{\text{AFM}} \sim 1/N$ [24, 31]. The numerical value of Δ_0 on finite-size systems can be computed in DMRG by solving for the lowest-energy state orthogonal to the previously obtained ground state, in the same $S^z = 0$ sector. We plot $\Delta_0(\delta)$ in Fig. 11c,d for both the $N = 42$ and $N = 100$ clusters. The behavior of $\Delta_0(\delta)$ differs somewhat from that seen in Sec. E1, due to a difference in boundary conditions (open instead of periodic). Across the phase diagram, $\Delta_0(\delta)$ is fairly large, which helps to explain the success of the adiabatic preparation: the ramp decay time scale, $\tau = 1.45 \hbar/J$, is slower than (FM) or approximately equal to (AFM) the inverse gap, $\Delta_0^{-1} = 0.45 \hbar/J$ (FM), $1.47 \hbar/J$ (AFM). The smaller gap for the antiferromagnet is a manifestation of its frustration, and makes adiabatically preparing its ground state more difficult compared to $H_{\text{XY}}^{\text{FM}}$. Comparing Δ_0 to the excess energy

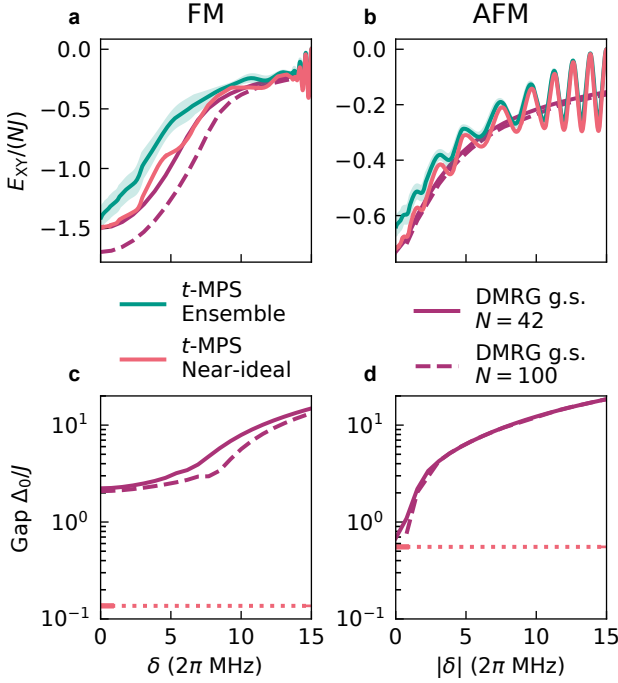


Figure 11. **Energetics of the simulated adiabatic preparation.** **a, b,** Interaction energy density $E_{XY}/N(\delta)$ in the t -MPS simulations of the 6×7 lattice. The teal line and envelope are the disorder ensemble average and standard deviation, respectively. Following a single state with minimal initialization errors (pink line), we see that E_{XY} tightly follows the DMRG ground state value (purple), confirming that diabatic errors are negligible. **c, d,** Energy gaps Δ_0 between the ground state and the first excited state in the $S^z = 0$ sector, obtained from DMRG. For the near-ideal initial state, the final energy density (pink dotted line) falls below the gap in both the FM and AFM case.

the end of the ramp, we find that the near-ideal initial state ends up with a total effective energy, $\mathcal{E} = NE_{XY}/N$, below the many-body gap. The difference is remarkably large for the ferromagnet ($\mathcal{E}/\Delta_0^{\text{FM}} = 0.06$), implying a near-flawless adiabatic sweep, while the margin for the antiferromagnet is much narrower ($\mathcal{E}/\Delta_0^{\text{AFM}} = 0.81$).

F. Thermal phase diagram

We conclude by discussing the phase diagram of $H_{XY} + H_Z$ at finite temperature, T (measured in unit of k_B). While two-dimensional, $U(1)$ -symmetric systems can have XY LRO ground states, for short-range interacting models such as H_{nn} this order does not persist to finite temperature [17–20]. Physically, this is because spin-wave excitations proliferate at finite temperature and destroy the XY order. Instead, most two-dimensional XY models have an *algebraic long-range ordered* phase at low temperatures, separated from the high- T disordered phase by a Berezinskii-Kosterlitz-Thouless (BKT) transition at a critical temperature T_{BKT} [39–42]. The low- T phase is characterized by power-law-decaying correlations, $C^x(d) \sim d^{-1/(2\pi K)}$, with a temperature-dependent exponent K that attains the universal value $K_{\text{BKT}} = 2/\pi$ at T_{BKT} .

For the classical nearest-neighbor XY model, $T_{\text{BKT}}^{\text{cl}}/(2J) = 0.892943(2)$ [65, 66], while in the quantum spin-1/2 H_{nn} the transition is lowered to $T_{\text{BKT}}^{\text{nn}}/(2J) = 0.353(3)$ [67, 68].

Long-range interactions can modify the spin-wave dispersion relation, suppressing their proliferation and thus renewing the possibility for XY LRO at finite temperature [24, 25, 31]. In 1976, Kunz and Pfister proved that the classical version of H_{XY}^{FM} indeed exhibits a first-order, finite-temperature phase transition between the high- T disordered phase and a low- T XY LRO phase [23]. Subsequent Monte Carlo simulations located this transition at $T_c^{\text{FM}}/(2J) = 3.96(4)$ [69, 70]. By contrast, for H_{XY}^{AFM} one expects the low- T physics to be similar to that of H_{nn} , although the location and critical properties of the BKT transition may be modified [21, 43].

1. Exact diagonalization phase diagram for $N = 16$

To probe the thermal properties of the $H = H_{XY} + H_Z$ model, we perform exact diagonalization on a small 4×4 lattice geometry and directly operate on the thermal density matrix $\rho \propto e^{-H/T}$. In Fig. 12a,b, we show 2D color plots of the squared magnetization $m_{\text{FM/AFM}}^2$ at finite T and δ . For the ferromagnet (Fig. 12a), we observe a lobe around $(T, \delta) = 0$ that corresponds to the XY-ordered phase. The order begins to disappear around $T/J = 1.5$ (for the thermal phase transition) and $\delta/J = 5$ (for the quantum phase transition). Examining m_{AFM}^2 for the AFM case (Fig. 12b), we observe a smaller lobe with apparent XY order. Although H_{XY}^{AFM} is not predicted to host true long range order at $T > 0$, obtaining $m_{\text{AFM}}^2 > 0$ is still possible on finite-size systems.

One way to identify the finite-temperature phase boundary is by a peak in the corresponding derivative, $-dm^2/dT$, which is shown in Fig 12c,d. Owing to the small system size, one finds a smooth crossover for both models, and it is difficult to ascertain what the nature of the phase transition may be in the thermodynamic limit. It should be possible to study larger system sizes for H_{XY}^{FM} using quantum Monte Carlo methods [71], which is beyond the scope of this work. For now, we cautiously estimate $T_{XY}^{\text{FM}}/J \approx 1.5$ and $T_{XY}^{\text{AFM}}/J \approx 0.6$, as the $\delta = 0$ crossover temperature into the low- T phase. Compared to H_{nn} , for which $T_{\text{BKT}}^{\text{nn}}/J = 0.706(6)$ [67, 68], the dipolar ferromagnet appears to have a higher transition temperature (although not as high as the classical model [69, 70]), while the antiferromagnet may have a slightly lower one.

2. Temperature calibration of ramps and quenches

With the thermal density matrix, $\rho \propto e^{-H/T}$, we also determine the temperature and δ dependence of the internal energy, $E(T) = \text{Tr}[\rho H]$. The inverse function $T(E)$ defines a temperature calibration: we estimate the effective temperature of a state from its energy density. Inputting the mean final energy density of our t -MPS simulations (Sec. E), we estimate the effective temperatures at the end of the adiabatic ramp to be $T_{\text{MPS}}^{\text{FM}}/J = 1.12$ and $T_{\text{MPS}}^{\text{AFM}}/J = 0.48$. The t -MPS disorder ensemble results in a spread of energies $E_{XY} \pm \sigma_E$; the

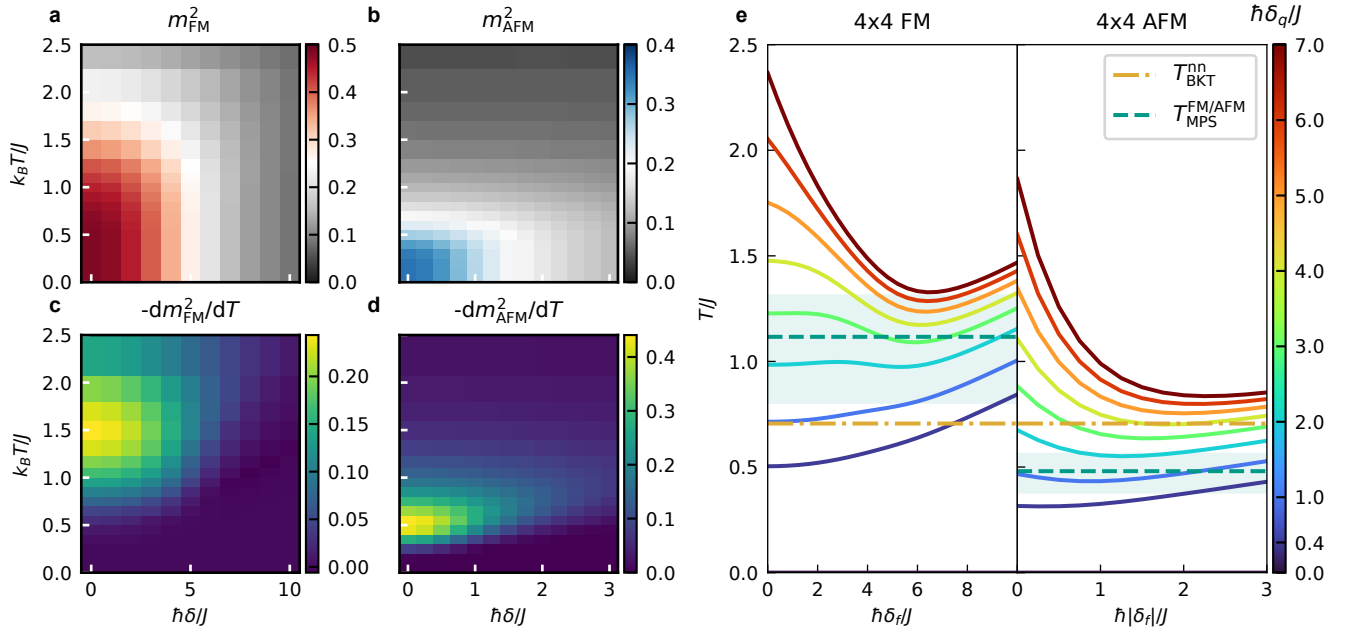


Figure 12. **Finite-temperature properties of $H_{XY} + H_Z$.** **a, b,** Phase diagrams of $H_{XY} + H_Z$ at finite temperature, T and light-shift δ , computed from exact diagonalization on a 4×4 array. The ferromagnet and antiferromagnet each exhibit a region with finite magnetization $m_{\text{FM/AFM}}^2$ at small δ and small T . In the thermodynamic limit, we expect these regions to become, respectively, the LRO and algebraic-ordered (BKT) phases. **c, d,** Estimate of the phase boundary from the mixed susceptibility, $-dm^2/dT$. At this system size, there are strong finite size effects that produce a smooth transition into the disordered phase. **e,** Estimated temperature of a quench experiment with final light-shift δ_f and quench magnitude δ_q . The behavior is nonlinear in δ_q and nonmonotonic in δ_f . For comparison, we also show the effective temperature corresponding to the ensemble E_{XY} at the end of the t -MPS adiabatic ramp simulation (teal; ensemble average as dashed line, standard interval as shaded region), as well as the BKT transition temperature $T_{\text{BKT}}^{\text{nn}}$ of the nearest-neighbor model, H_{nn} (yellow dashed line).

corresponding temperature intervals are $T_{\text{MPS}}^{\text{FM}} \in [0.81, 1.31]$ and $T_{\text{MPS}}^{\text{AFM}} \in [0.38, 0.56]$. These intervals are asymmetric about the mean value due to the nonlinearity of $T(E)$. As discussed in Sec. E3, the final energy densities – and hence effective temperature – are dominated by errors in the initial state, although diabatic errors may become more important for larger systems. The obtained values T_{MPS} are near, but somewhat below, the respective transition temperatures T_{XY} estimated in the previous section. However, temperatures obtained for $N = 16$ calibration are not necessarily reliable due to the small system size, and should be considered as an order-of-magnitude estimate.

Performing an analogous temperature calibration at finite δ , we also estimate the effective temperatures produced by the quantum quench experiments (main text Fig. 1c,e,f), with

final light-shift δ_f and quench magnitude δ_q . We compute this temperature assuming *perfect* adiabatic preparation up to the pre-quench field $\delta_f + \delta_q$, i.e. by evaluating the energy $\langle H_{XY} + H_Z(\delta_f) \rangle$ in the *ground state* of $H_{XY} + H_Z(\delta_f + \delta_q)$ and then converting it to a temperature. Figure 12e shows the effective temperature T at different magnitudes of the quench δ_q as a function of the final light-shift δ_f . Notably, the effective temperature increases rapidly for small values of δ_q and slows down at larger values of δ_q for both the FM and AFM cases. Additionally, the effective temperature produced by a fixed quench δ_q varies considerably depending on the endpoint δ_f . Again, the small system size of $N = 16$ means the quantitative δ to T correspondence may be unreliable, although it is likely that these trends remain accurate.